

ADVANCED MATERIALS

Supporting Information

for *Adv. Mater.*, DOI 10.1002/adma.202304986

A Mediator-Free Multi-Ply Biofuel Cell Using an Interfacial Assembly between Hydrophilic Enzymes and Hydrophobic Conductive Oxide Nanoparticles with Pointed Apexes

Minchul Kang, Donghyeon Nam, Jeongyeon Ahn, Yoon Jang Chung, Seung Woo Lee, Young-Bong Choi, Cheong Hoon Kwon and Jinhan Cho**

Supporting Information

A Mediator-Free Multi-ply Biofuel Cell Using an Interfacial Assembly between Hydrophilic Enzymes and Hydrophobic Conductive Oxide Nanoparticles with Pointed Apexes

Minchul Kang[§], Donghyeon Nam[§], Jeongyeon Ahn[§], Yoon Jang Chung, Seung Woo Lee, Young-Bong Choi, Cheong Hoon Kwon, and Jinhan Cho**

[§]These authors equally contributed to this work.

Experimental Section

Materials: Cotton fibrils with a diameter of 200 μm were purchased from Igonji, Carbon nanotubes (MWCNT with a diameter of 7~9 nm, a length of 10~50 μm , and a purity of >80 %) were purchased from Uniam Co.Ltd(South Korea). Glucose oxidase (GOx) from *Aspergillus niger* (180 U mg^{-1}) was purchased from Amano Enzyme Inc. (Japan). Tetraoctylammonium bromide (TOABr), gold(III) chloride trihydrate ($\text{HAuCl}_4 \cdot 3\text{H}_2\text{O}$), sodium borohydride (NaBH_4), tris-(2-aminoethyl)amine (TREN) ($M_w \sim 146 \text{ g mol}^{-1}$) and polyethylenimine, branched (PEI, $M_w \sim 800 \text{ g mol}^{-1}$), Indium(III) acetate, tin(II) 2-ethylhexanoate, dioctyl ether, n-octanoic acid, and oleylamine, were purchased from Sigma-Aldrich.

Synthesis of COOH-MWCNT: Carboxylic acid-functionalized MWCNTs (COOH-MWCNTs) were prepared by subjecting pristine MWCNTs to strong acid treatment using $\text{H}_2\text{SO}_4/\text{HNO}_3$ at 75 $^\circ\text{C}$ for 2.5 h. The resulting COOH-MWCNTs were purified through centrifugation and vacuum filtration to remove the residual acid. As-prepared COOH-MWCNTs were redispersed in ethanol.

Synthesis of TOABr-Au NP: TOABr-stabilized Au NP (TOABr-Au NP) with a diameter of 8 nm were synthesized using a two-phase method in toluene.^[S1] Firstly, H₂AuCl₄·3H₂O in deionized water (30 mmol L⁻¹, 30 mL) and TOABr in toluene (20 mmol L⁻¹, 80 mL) were mixed with vigorous stirring, and then NaBH₄ in water (0.4 mol L⁻¹, 25 mL) was added to the two-phase mixture. After stirring for approximately 3 h, the aqueous solution was separated from the mixture, and the remaining toluene solution was repeatedly washed with dilute aqueous H₂SO₄ (0.1 mol L⁻¹), NaOH (0.1 mol L⁻¹), and deionized water. After several washing steps and the removal of the aqueous solution, TOABr-Au NP dispersed in toluene were obtained.

Synthesis of OAm-Indium Tin Oxide NP: OAm-ITO NP with a diameter of approximately 7 nm were prepared in toluene using a method reported by Kanehara *et al.*^[S2] Briefly, indium(III) acetate (1.08 mmol) and tin(II) 2-ethylhexanoate (0.12 mmol) were added to a dioctyl ether (10 mL) solution containing n-octanoic acid (3.6 mmol) and OAm (30 mmol). The resulting reaction mixture was stirred at 80 °C for 30 min. After the mild heating process, the mixture was heated at 150 °C for 1 h under an argon atmosphere, and then heated again at 280 °C for 2 h. After these successive heating processes, the reaction mixture was slowly cooled to room temperature and purified with excess acetone using centrifugation several times. Finally, the obtained OAm-ITO NPs were dispersed in toluene.

Preparation of n-(COOH-MWCNT/TREN)/fiber electrode: Cotton fibers composed of hydroxy (OH) group-functionalized cellulose were immersed in 1 mg mL⁻¹ ethanolic solutions of amine (NH₂)-functionalized PEI (Mw ~800) for 2 h. The resulting PEI-coated fibers were prepared through a hydrogen-bonding interaction between the NH₂ of PEI and the OH groups of the cotton fibers. Next, the PEI-coated fibers were dipped in a COOH-MWCNT solution for 10 min and then washed with ethanol to remove the weakly absorbed COOH-MWCNT. The resulting COOH-MWCNT coated cotton fibers were then immersed in a 2 mg mL⁻¹ ethanol solution of TREN for 10 min and washed with pure ethanol. As a result, the

carboxyl group, which acts as a functional group for MWCNT, binds to the NH_2 group of TREN through hydrogen bonding, resulting in fibers coated with one bilayer (i.e., 1-MWCNT/fiber). This deposition method of (COOH-MWCNT/TREN) was repeated 10 times to produce (COOH-MWCNT/TREN)₁₀ onto cotton fiber, resulting in 10-MWCNT/fiber with resistivity of $\sim 0.1 \Omega \text{ cm}^{-1}$.

Preparation of 20-Au-MWCNT/fiber electrode: To prepare a metallic cotton fiber electrode, the 10-MWCNT/fiber was immersed in a 5 mg mL^{-1} solution of TOABr-Au NP for 40 min and then washed with toluene to remove the weakly adsorbed TOABr-Au NP. In this case, the bulky TOABr ligands bound to the surface of the Au NP were almost completely replaced by NH_2 groups of the TREN-coated fibers due to the high affinity between the Au surface and NH_2 groups. Next, the resulting TOABr-Au NP-coated fibers were immersed in a 2 mg mL^{-1} solution of TREN in ethanol for 40 min. This process was repeated, and the fibers were washed with ethanol to remove excess TREN molecules, resulting in fibers coated with one bilayer (i.e., 1-Au-MWCNT-fiber). The adsorption mechanism between the TOABr-Au NP and the NH_2 -functionalized TREN is the same as that between the TOABr-Au NP and PEI. These depositions and washing steps for the preparation of the cotton fiber electrode were continuously repeated until the desired number of bilayers was obtained.

Preparation of anode: To prepare the CF electrode with the outermost NH_2 -functionalized TREN layer, we first immersed it in a toluene solution containing OAm-ITO NPs at a concentration of 5 mg mL^{-1} for 20 min. Afterward, the electrode was rinsed with toluene to eliminate any loosely attached OAm-ITO NPs. This step facilitated the replacement of the bulky OAm ligands on the ITO NPs with NH_2 groups from the TREN-coated CF electrodes. Next, the CF electrode, now with OAm-ITO NPs adsorbed on the outermost layer, was submerged in a 5 mg mL^{-1} solution of GOx in PBS (pH 7.4) for 10 min, followed by washing with PBS to remove any weakly adsorbed GOx. During this process, the amino acid groups in GOx, containing NH_2 and COOH moieties, directly bonded to the surface of the ITO NPs,

effectively replacing the previously attached bulky OAm ligands. These depositions and washing steps were repeated as necessary until the desired number of bilayers had been achieved. In addition, for anodes made by crosslinking method (i.e., (GOx/PEGDGE) slurry/CF), the CF host electrode was dip-coated into a solution composed of GOx (95 wt%) and PEGDGE (5 wt%) in DI.

Preparation of cathode:

To prepare the cathode for BFCs, a vacuum sputtering process was used to deposit Pt onto the CF electrode. This process utilized an ion sputter coater (MC1000, Hitachi) with argon (Ar) gas flow, and a discharge current of 20 mA. The duration of sputtering was adjusted, with a maximum sputtering time of 90 seconds.

Characterization and analysis of Au-MWCNT/fiber electrode:

The surface and cross-sectional morphologies of the CF-based BFCs electrodes were characterized using FE-SEM (Hitachi S4800, Japan). The adsorption behavior and mechanism of formation of the (TOABr-Au NP/TREN)_m multilayers were investigated using FTIR spectroscopy in specular mode. The growth and loading amount of the LbL-assembled multilayers were examined using UV-Vis spectroscopy on quartz glass, and a QCM (QCM 200, SRS, USA), respectively. In the case of QCM measurement, the mass change (ΔM) per layer was calculated from the QCM frequency change (ΔF) using the Sauerbrey equation,^[S3,S4]

$$\Delta F(\text{Hz}) = -\frac{2F_0^2}{A\sqrt{\rho_q\mu_q}} \cdot \Delta M$$

where F_0 , A , ρ_q , and μ_q represent the resonant frequency (~5 MHz), the active area (cm²), the density (2.65 g cm⁻³), and the shear modulus (2.95×10¹¹ g cm⁻¹ s⁻²) of the QCM electrode, respectively. This expression can be simplified to ΔF (Hz) = -56.6 × ΔMA (MA indicates mass per unit area).

Electrochemical measurements:

A three-electrode system composed of a CF working electrode, an Ag/AgCl reference electrode, and a Pt counter electrode was used. The top end of the working electrode was firmly connected to a copper wire using commercial silver paste (ELCOAT P-100, CANS, South Korea), and once the silver paste had dried, it was further insulated with an epoxy adhesive. Cyclic voltammograms were obtained for the CF electrode, which had a diameter of 200 μm , length of 1.0 mm, and active external surface area of 6.28 mm^2 , over the potential range of -0.6 to $+0.6$ V, using an electrochemical analyzer (Ivium-n-Stat, Ivium Technologies, Netherlands). All measurements were conducted in an electrochemical cell in batch mode, with 50 mL of PBS buffer (20 mmol L^{-1} phosphate and 0.14 mol L^{-1} NaCl, pH 7.4) at 36.5 $^{\circ}\text{C}$, without stirring. The interelectrode spacing between the anode and cathode electrode was ~ 1 cm, and no membrane was used in this study.

Furthermore, to avoid electrical short circuit during power density measurement with continuous operation, epoxy resin was used to secure one end of each BFC electrode to the glass substrate. The anodic and cathodic current densities were calculated using CV at a fixed voltage of $+0.6$ V for the anode and -0.6 V for the cathode, respectively, which displayed the highest current density. To calculate the normalized current density, the current density level in glucose-free PBS was subtracted from the $+0.6$ V of anodic current density level, and the current density level in oxygen-free PBS was subtracted from the -0.6 V of cathodic current density level. The BFC power densities were measured by controlling cell potential and measuring the current output with a fixed external resistance (ranging from 1 $\text{k}\Omega$ to 10 $\text{M}\Omega$). Electrochemical impedance spectroscopy (EIS) measurements were conducted for the BFC electrodes using a perturbation amplitude of 0.01 V over a frequency range of 0.2 Hz to 100 kHz. The Nyquist plots of the real (Z') and imaginary parts (Z'') of the impedance spectra obtained from the electrochemical BFC cell were analyzed using ZView software (ver. 2.8d, Scribner Associates Inc., USA).

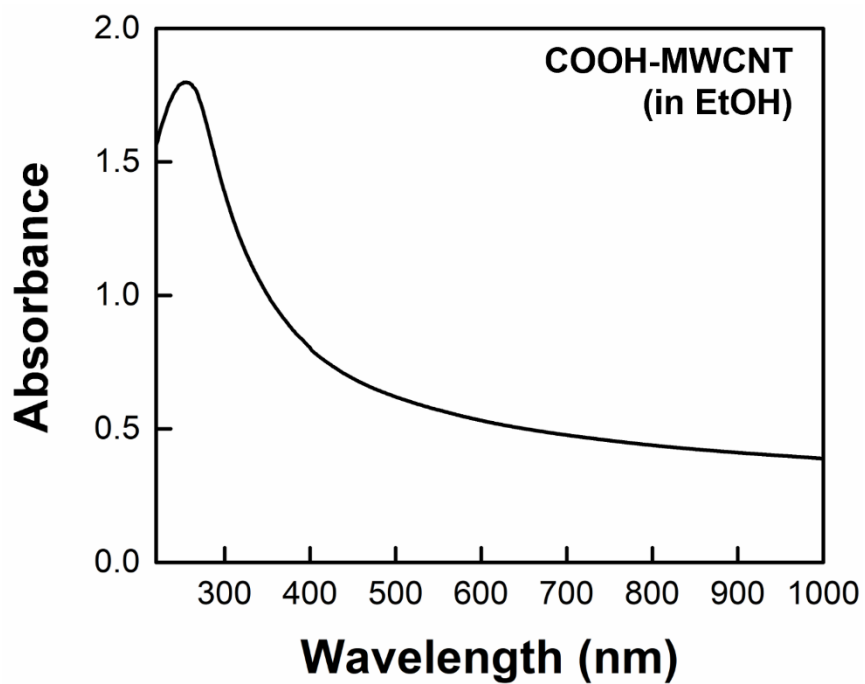


Figure S1. UV-vis spectrum of COOH-MWCNT dispersed in EtOH.

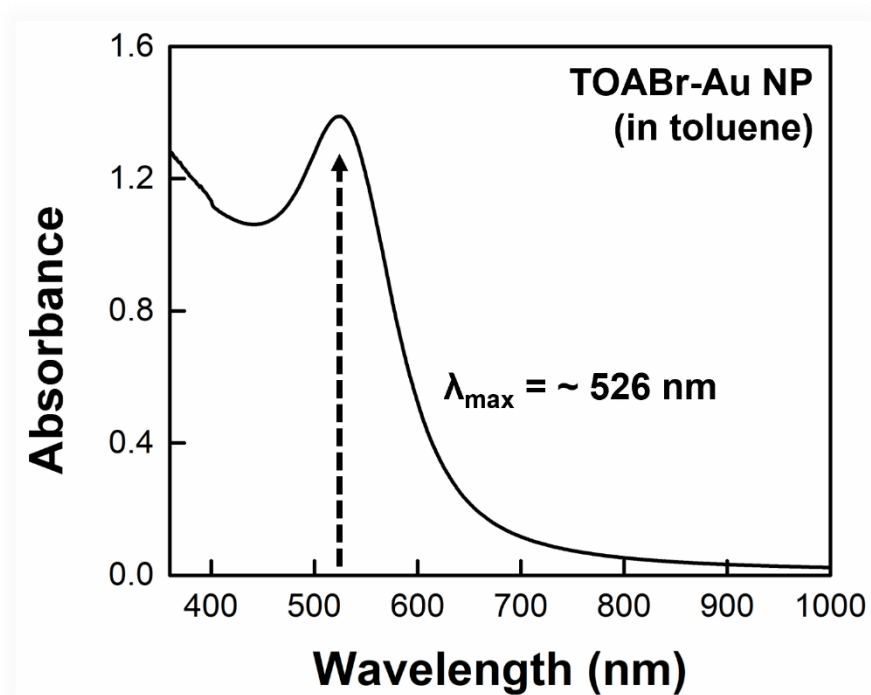


Figure S2. UV-vis spectrum of TOABr-Au NP (in toluene) with a surface plasmon absorption peak (λ_{\max}) of $\sim 526 \text{ nm}$.

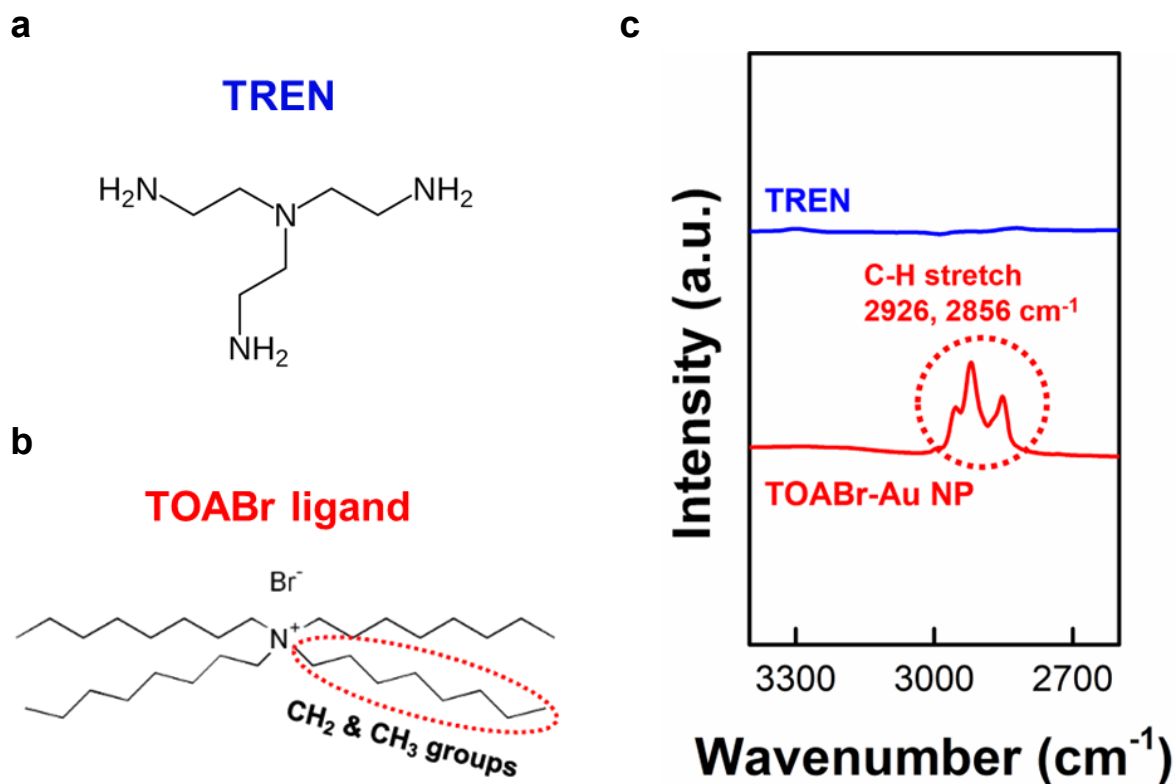


Figure S3. FTIR spectra of TOABr-Au NP and TREN. The molecular structure of a) TREN and b) TOABr ligands. c) The C-H stretching peak of TOABr ligands with long alkyl chains produced a significant absorbance peak at 2926 and 2856 cm⁻¹ in the TOABr-Au NP solution. This peak was used to investigate the ligand replacement reaction between the TOAB ligand and the NH₂ groups of TREN during repetitive LbL-assembly.

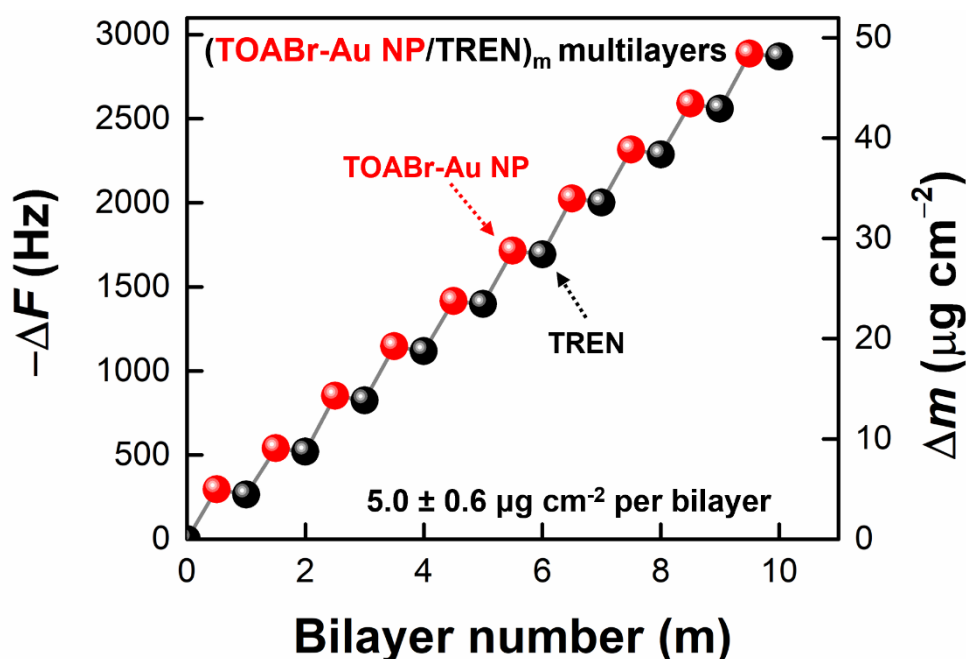


Figure S4. Quartz crystal microbalance analysis (QCM). The number of bilayers (m) in (TOABr-Au NP/TREN)_m multilayers was varied and the resulting changes in frequency (-ΔF) and mass (Δm) were analyzed using QCM. Mass changes per layer were determined by applying the Sauerbrey equation to the frequency changes of the TOABr-Au NP and TREN layers adsorbed on the QCM electrode. The (TOABr-Au NP/TREN)₂₀ multilayer had a total loading amount of approximately 50 μg cm⁻², as measured experimentally. During the deposition of TREN, a slight decrease in mass changes was observed, indicating the replacement of bulky TOABr (Mw ~547) ligands by much smaller TREN molecules (Mw ~146).

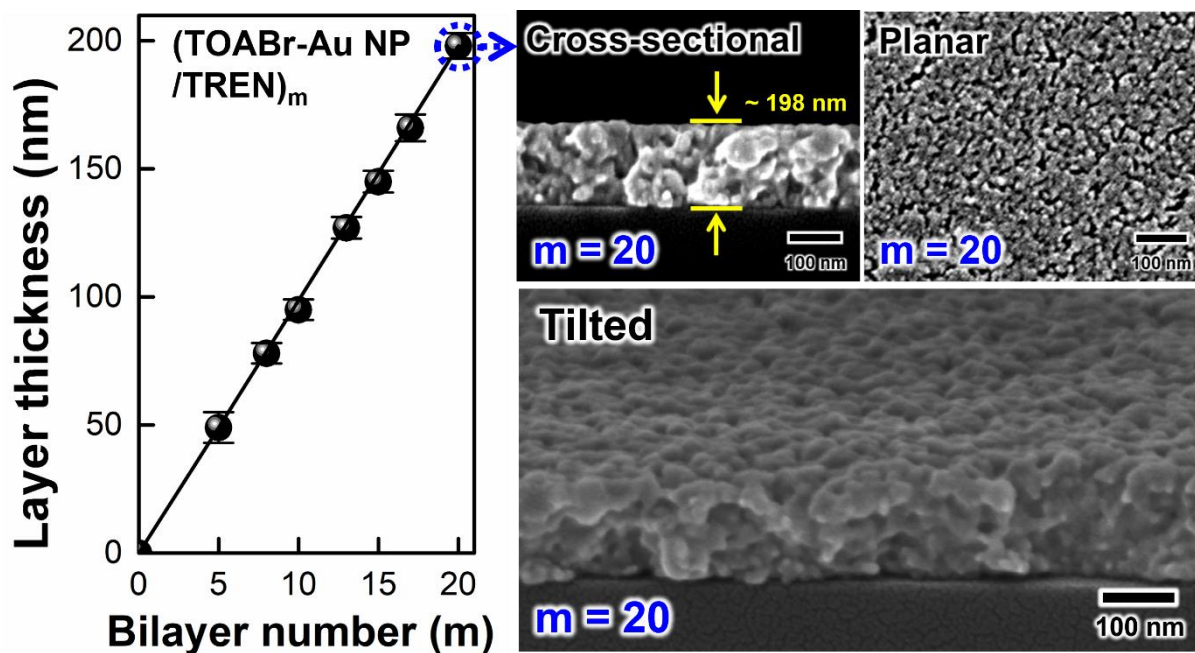


Figure S5. Characterization of $(\text{TOABr-Au NP/TREN})_m$ multilayers. Film thickness of $(\text{TOABr-Au NP/TREN})_m$ multilayers as a function of the bilayer number (left image) and cross-sectional/planar/tilted FE-SEM images of $(\text{TOABr-Au NP/TREN})_{20}$ multilayers (right). The multilayers were fabricated using Layer-by-Layer-assembly, and the film thickness measured using a FE-SEM.

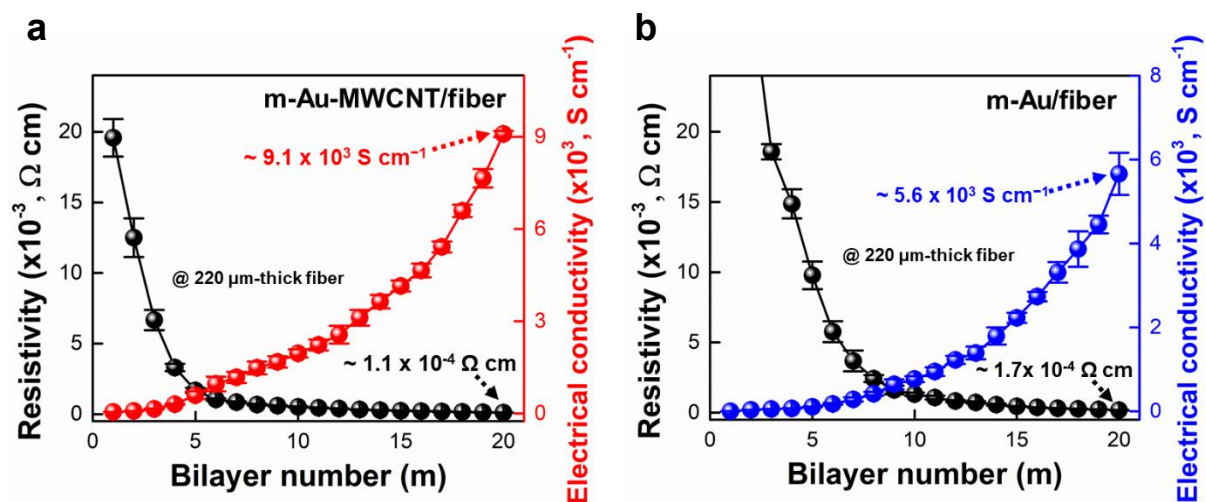


Figure S6. Electrical properties of multilayered m-Au-MWCNT/fiber and m-Au/fiber electrodes. Resistivity and electrical conductivity of a) m-Au-MWCNT/fiber, and b) m-Au/fiber as a function of bilayer number (m). The error bars show the standard deviation from the mean value of electrical conductivity for three independent experiments.

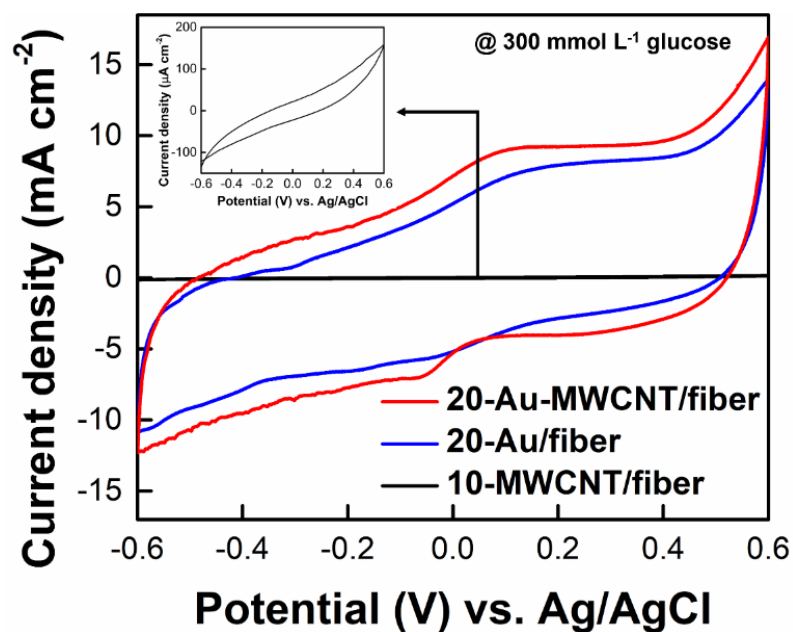


Figure S7. Electrochemical performance of three different host electrodes: 20-Au-MWCNT/fiber, 20-Au/fiber, and 10-MWCNT/fiber. CV curves for each electrode were measured in 20 mmol L⁻¹ phosphate-buffered saline (PBS) solution containing 300 mmol L⁻¹ glucose under ambient conditions and all measurements were performed at a scan rate of 5 mV s⁻¹.

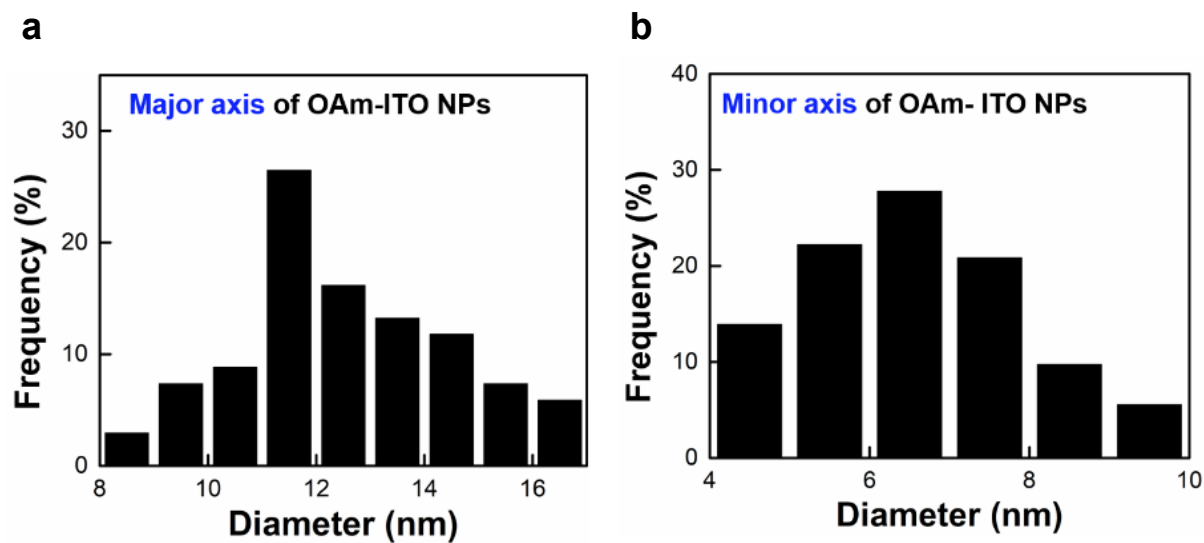


Figure S8. Size distribution of anisotropic branched OAm-ITO NPs measured by major and minor axis. a) Major axis and b) minor axis of the OAm-ITO NPs were determined by analyzing HR-TEM images, and the size distribution was obtained from statical analysis of the measurements.

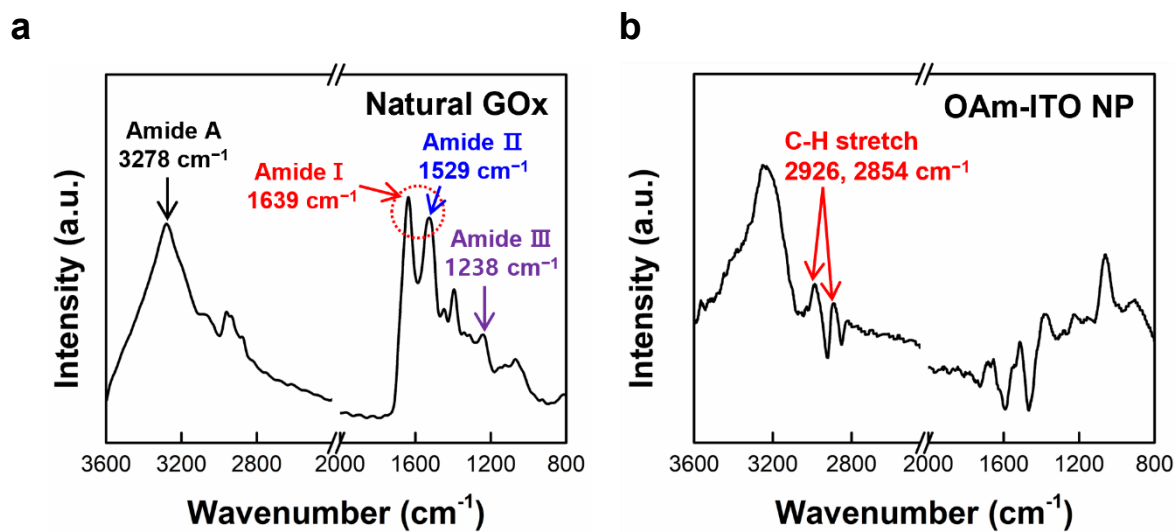


Figure S9. FTIR spectra of natural GOx and OAm-ITO NP. a) Characteristic FTIR spectra of native GOx^[S5-S7] and b) FTIR spectrum of OAm-ITO NP on Au-sputtered Si-wafer. In these cases, the native GOx and OAm-ITO NP were prepared by drop casting method, respectively.

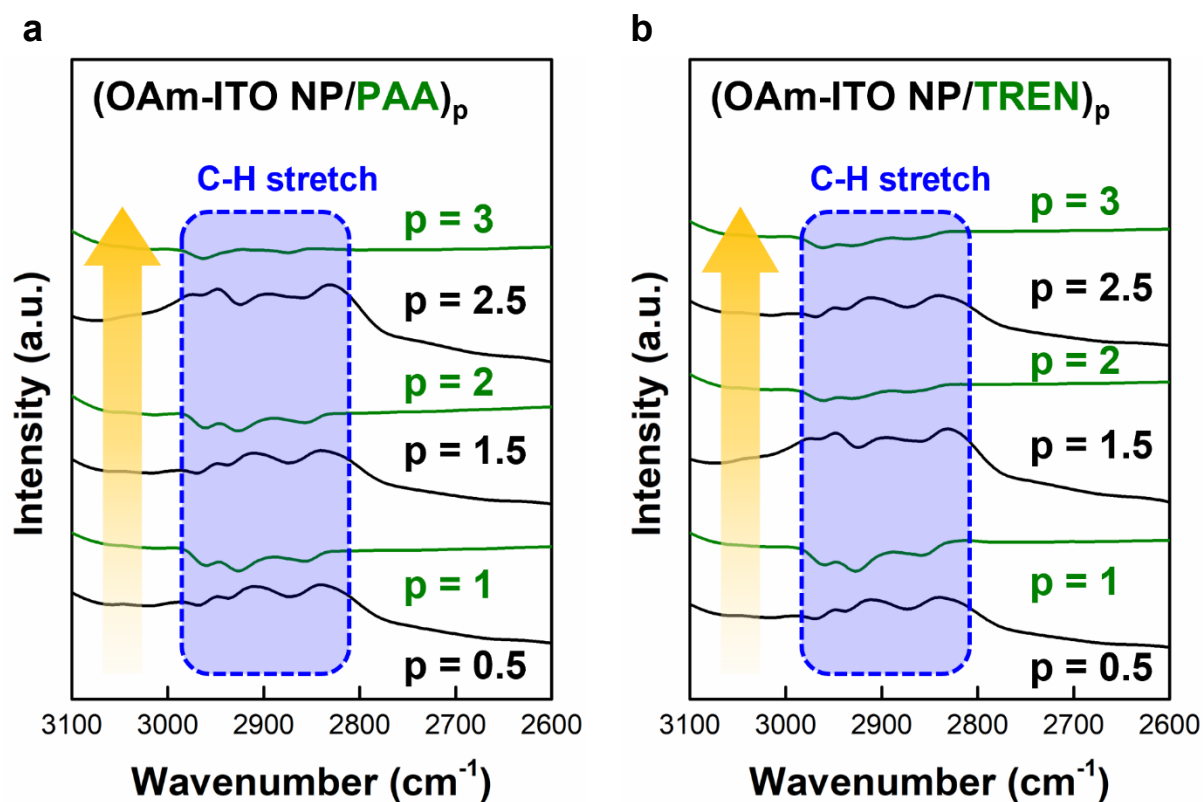


Figure S10. FTIR spectra of OAm-ITO NP with COOH- and NH_2 -functionalized linker. The spectra show the combination between OAm, the ligand of ITO NP, and a) (i.e., poly(acrylic acid) (PAA) and b) NH_2 -functionalized linker (i.e., TREN) as a polymeric linker.

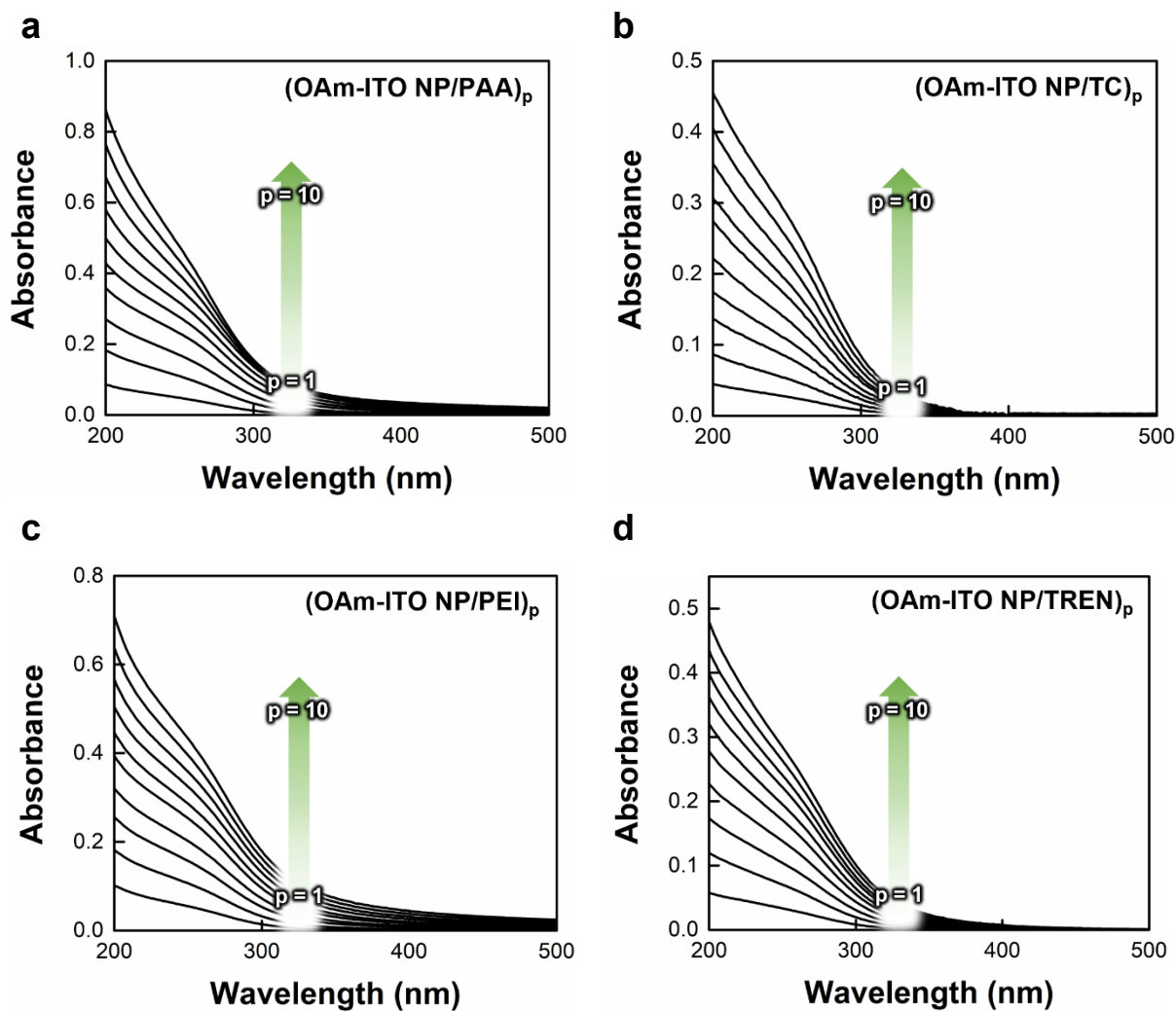


Figure S11. UV-vis absorbance spectra multilayers assembled onto a quartz substrate. The multilayers consist of a) (OAm-ITO NP/PAA)_p, b) (OAm-ITO NP/TC)_p, c) (OAm-ITO NP/PEI)_p and d) (OAm-ITO NP/TREN)_p as a function of bilayer number (p). The absorbance spectra were measured to investigate the growth and optical properties of the multilayers.

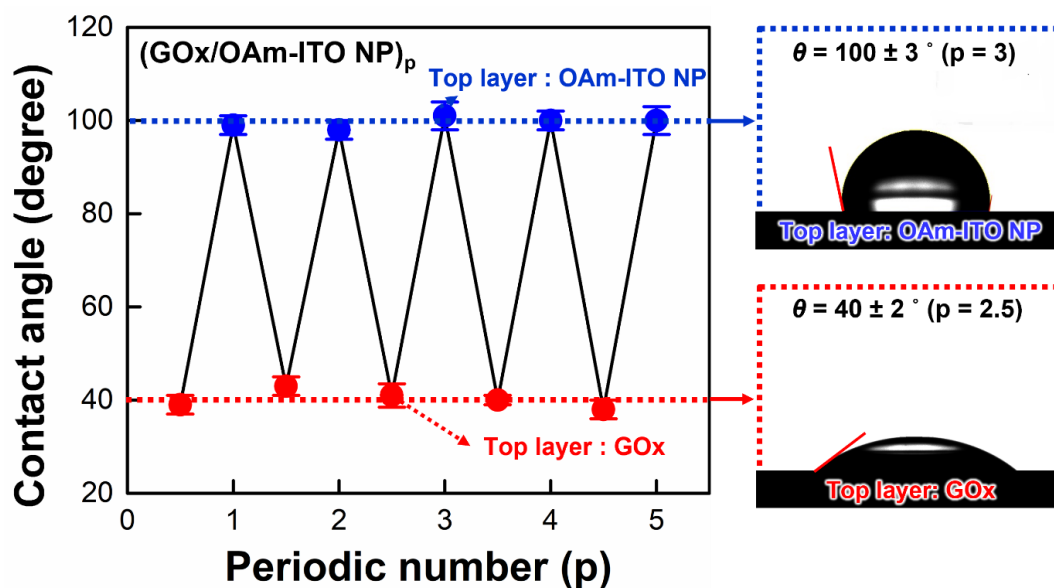


Figure S12. The deposition mechanism of $(\text{GOx}/\text{OAm-ITO NP})_p$ multilayers was analyzed using photographs of water droplets with contact angles (θ) on an Au-sputtered Si-wafer. The photographs show water droplets on multilayers with $(\text{GOx}/\text{OAm-ITO NP})_{p=2.5}$ and $(\text{GOx}/\text{OAm-ITO NP})_{p=3}$. As a result, the outermost GOx-coated $(\text{GOx}/\text{OAm-ITO NP})_{p=2.5}$ exhibited hydrophilic surface properties with a relatively lower contact angle of $\sim 40^\circ$ compared to the outermost OAm-ITO NP coated with a contact angle of $\sim 100^\circ$. The error bars indicated standard deviation from the mean value of contact angle for three independent experiments.

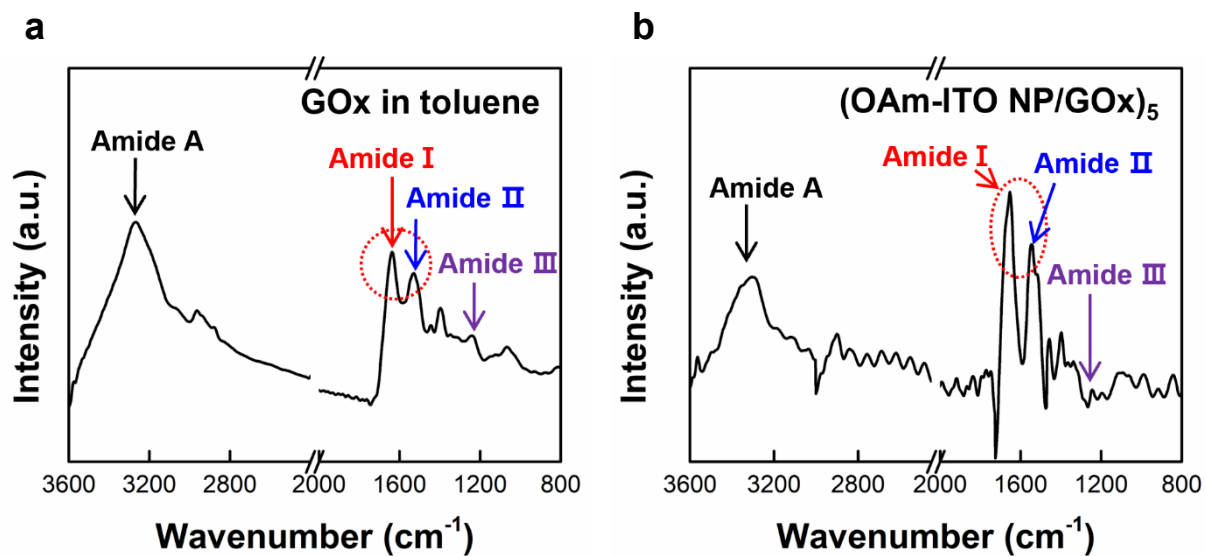


Figure S13. FTIR spectra of LbL-assembled $(\text{OAm-ITO/GOx})_5$ multilayers. a) Native GOx after immersing in toluene for 40 min and b) $(\text{OAm-ITO NP/GOx})_5$ multilayers deposited onto the Au-sputtered Si-wafer.

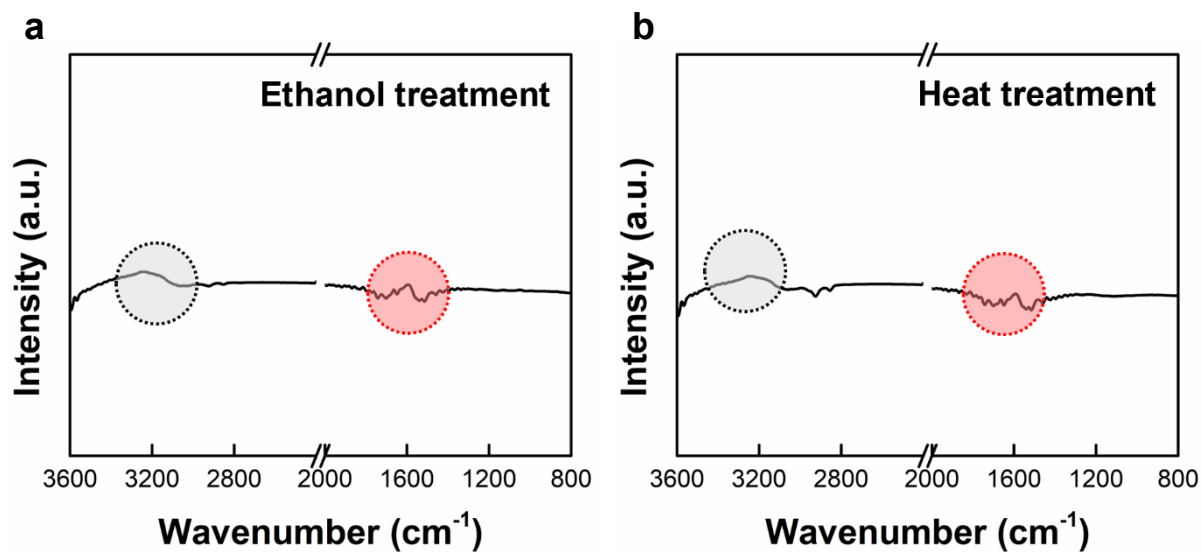


Figure S14. FTIR spectra of ethanol- and heat-treated GOx samples. FTIR spectra of GOx samples after immersing each into a) ethanol and b) boiling water of 100 °C for 20 min. The GOx samples were prepared by dropcasting native GOx onto Au-sputtered Si-wafer.

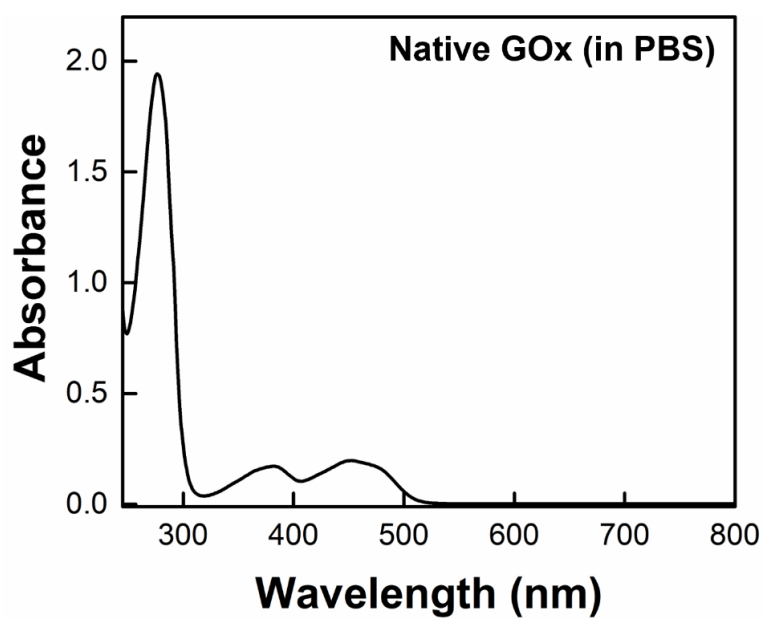


Figure S15. UV-vis spectrum of GOx dispersed in 20 mmol L⁻¹ PBS solution with a notable absorption peak at 277 nm.^[S8]

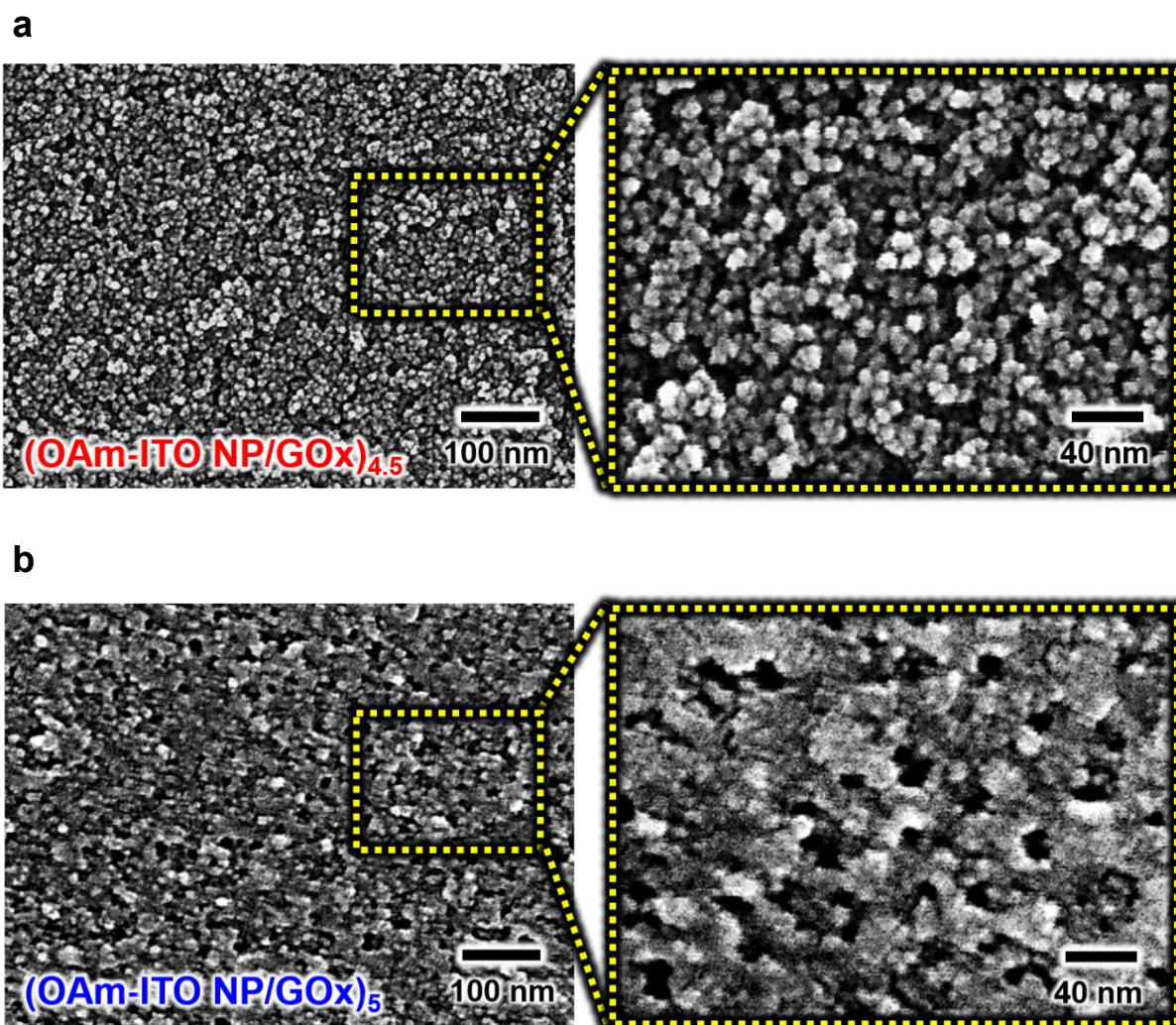


Figure S16. Planar FE-SEM image of a) (OAm-ITO NP/GOx)_{4.5} and b) (OAm-ITO NP/GOx)₅ multilayer on Si wafer, showing the surface morphology. GOx and OAm-ITO NP layers were uniformly adsorbed onto each other through LbL assembly.

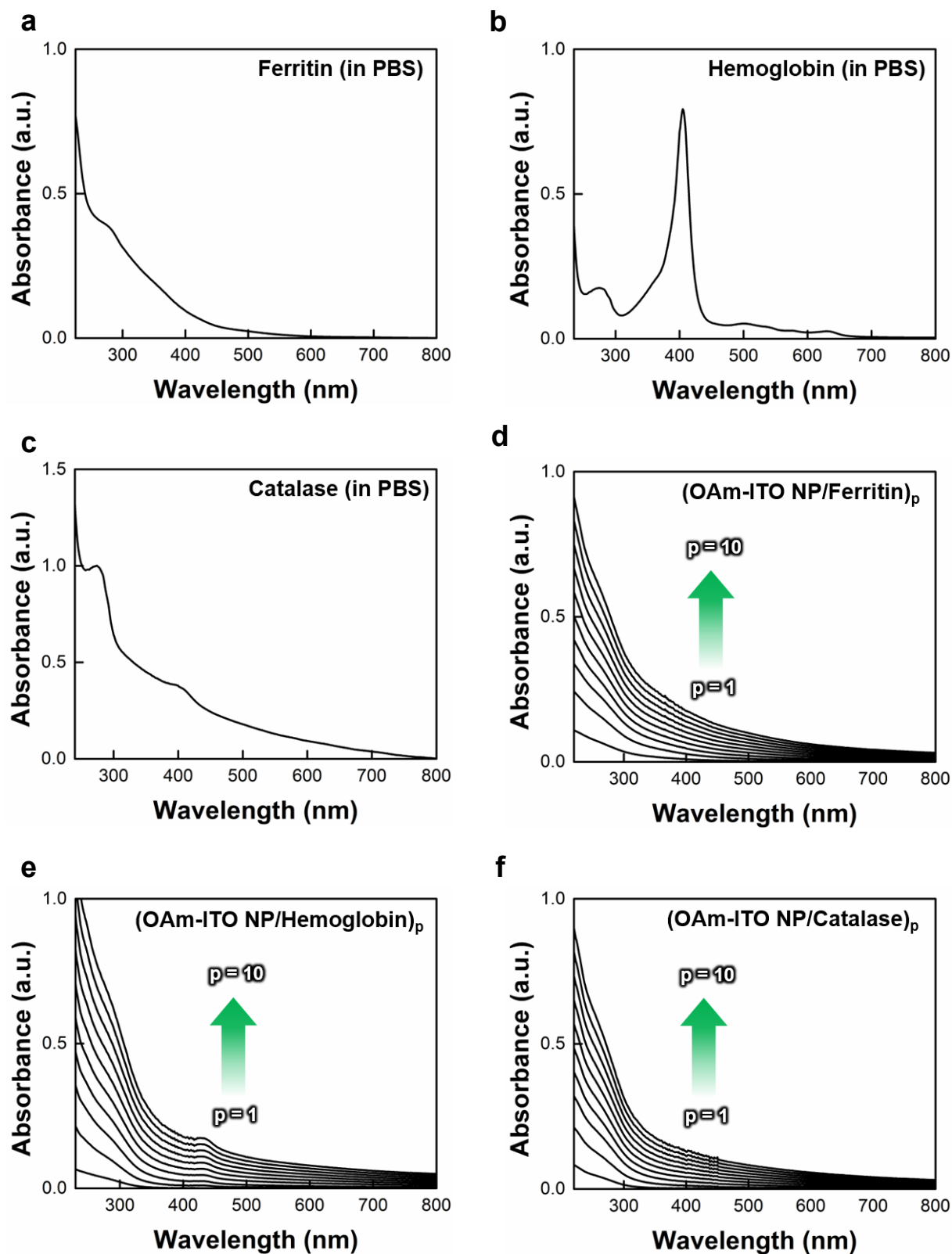


Figure S17. UV-Vis spectra of the a) ferritin, b) hemoglobin, c) catalase, d) (OAm-ITO NP/Ferritin)_p, e) (OAm-ITO NP/Hemoglobin)_p, and f) (OAm-ITO NP/Catalase)_p multilayers as a function of the bilayer number (p) from 1 to 10.

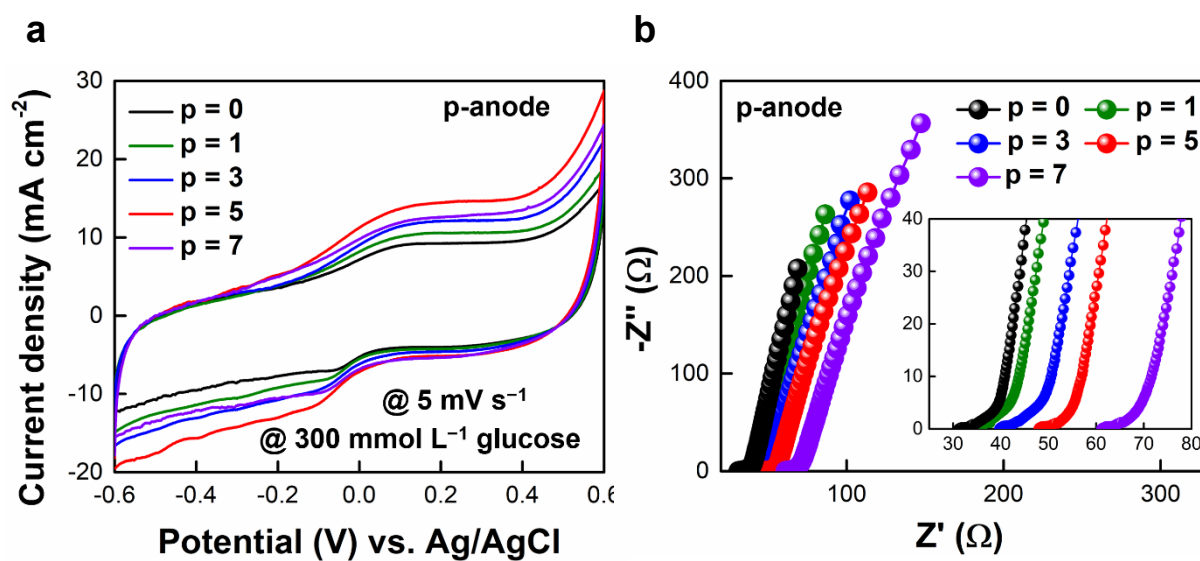


Figure S18. Electrochemical performance of the p-anode. a) Cyclic voltammetry and b) Nyquist plots of p-anode as increasing bilayer number ($p = 1, 3, 5$ and 7). Inset: Nyquist plots magnified in the high-frequency range. In this case, Figure S18 b) show that as the bilayer number increases, the equivalent series resistance (ESR) value also increased from 35.3 to 62.4Ω , respectively. All measurements were performed at a scan rate 5 mV s^{-1} in PBS under ambient conditions.

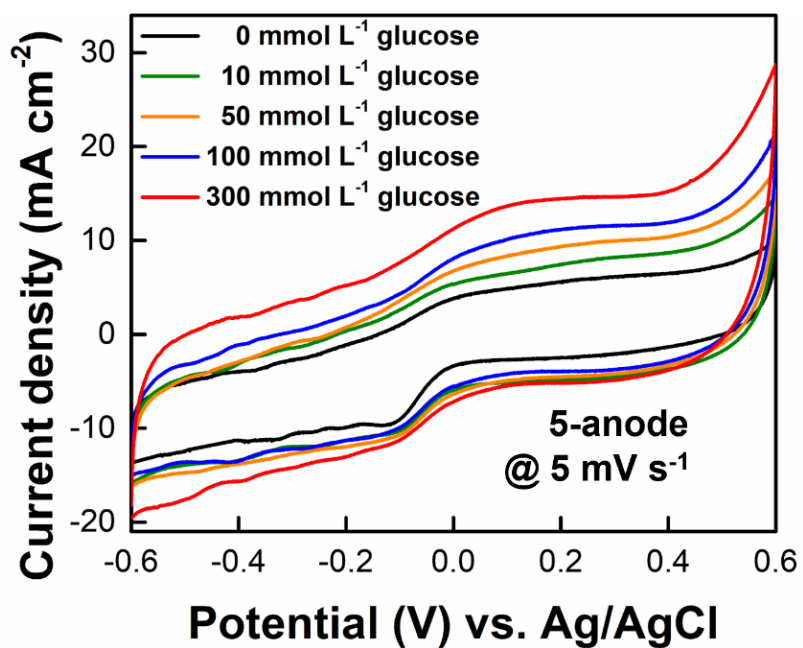


Figure S19. CV curves of 5-anode as a function of glucose concentration. The CV curves demonstrate the electrochemical performance of the 5-anode and how current density change in response to increasing concentrations of glucose.

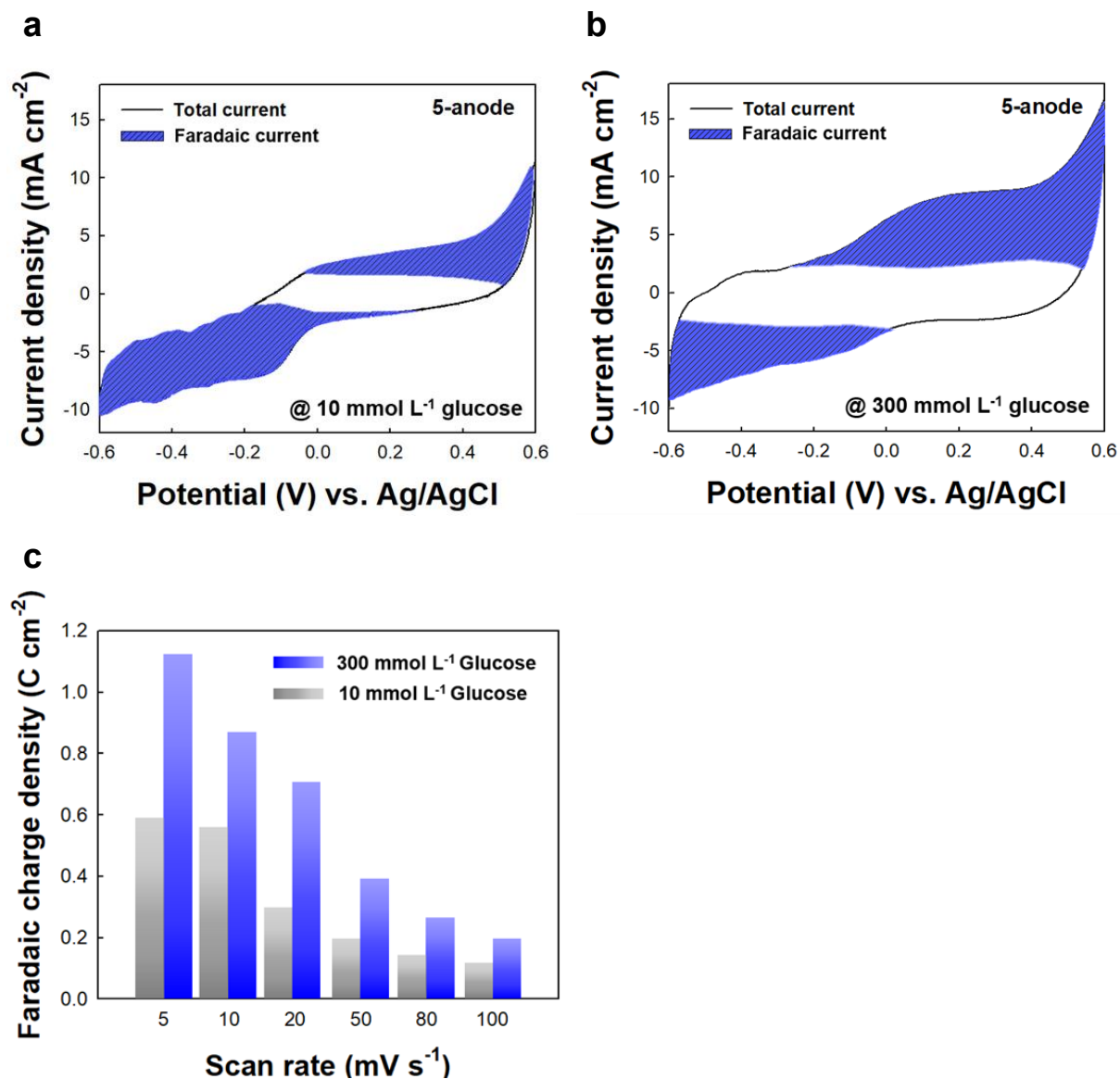


Figure S20. Analysis of charge contribution of the 5-anode through Dunn's method. CV curves of 5-anode at scan rate of 5 mV s⁻¹ deconvoluted into Faradaic-contributed sections in the glucose concentration of a) 10 and b) 300 mmol L⁻¹. c) Charge contribution of the 5-anode in different glucose concentration at a various scan rate ranging from 5 to 100 mV s⁻¹.

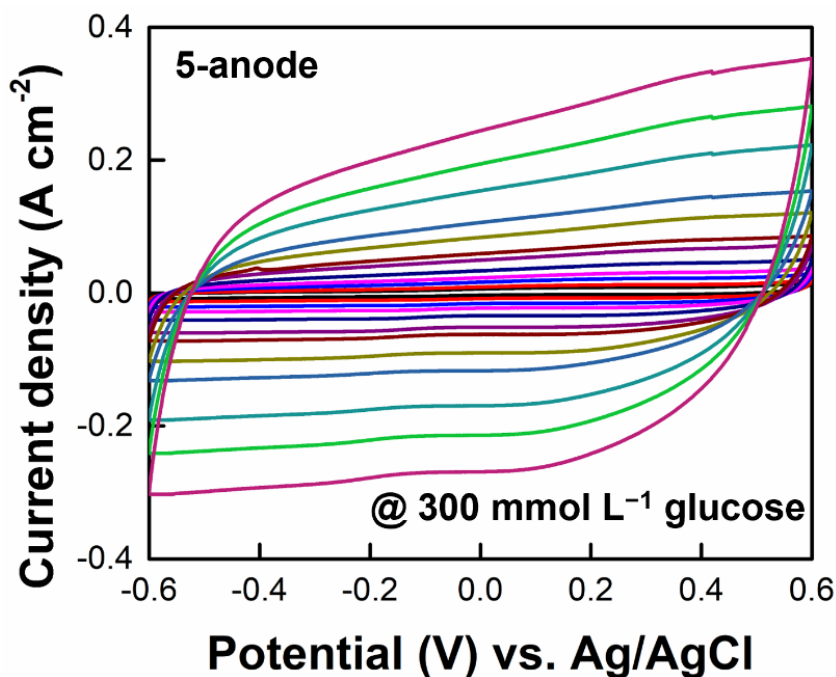


Figure S21. Electrochemical response of the of 5-anode. Cyclic voltammetry curve of the 5-anode in the 300 mmol L⁻¹ glucose in PBS at different scan rates 0.005, 0.01, 0.02, 0.04, 0.05, 0.08, 0.1, 0.15, 0.2, 0.3, 0.4, 0.5 V s⁻¹, respectively. A large K_s means that it can effectively promote electron transfer of the enzyme GOx and the electrode.^[S9,S10] The K_s value of the anode was calculated from the plot of the separation potential ($\Delta E_p = E - E^{0'}$) vs. $\ln \nu$ at high scan rates. The 5-anode exhibited a high K_s value of 6.3 ± 0.1 s⁻¹.

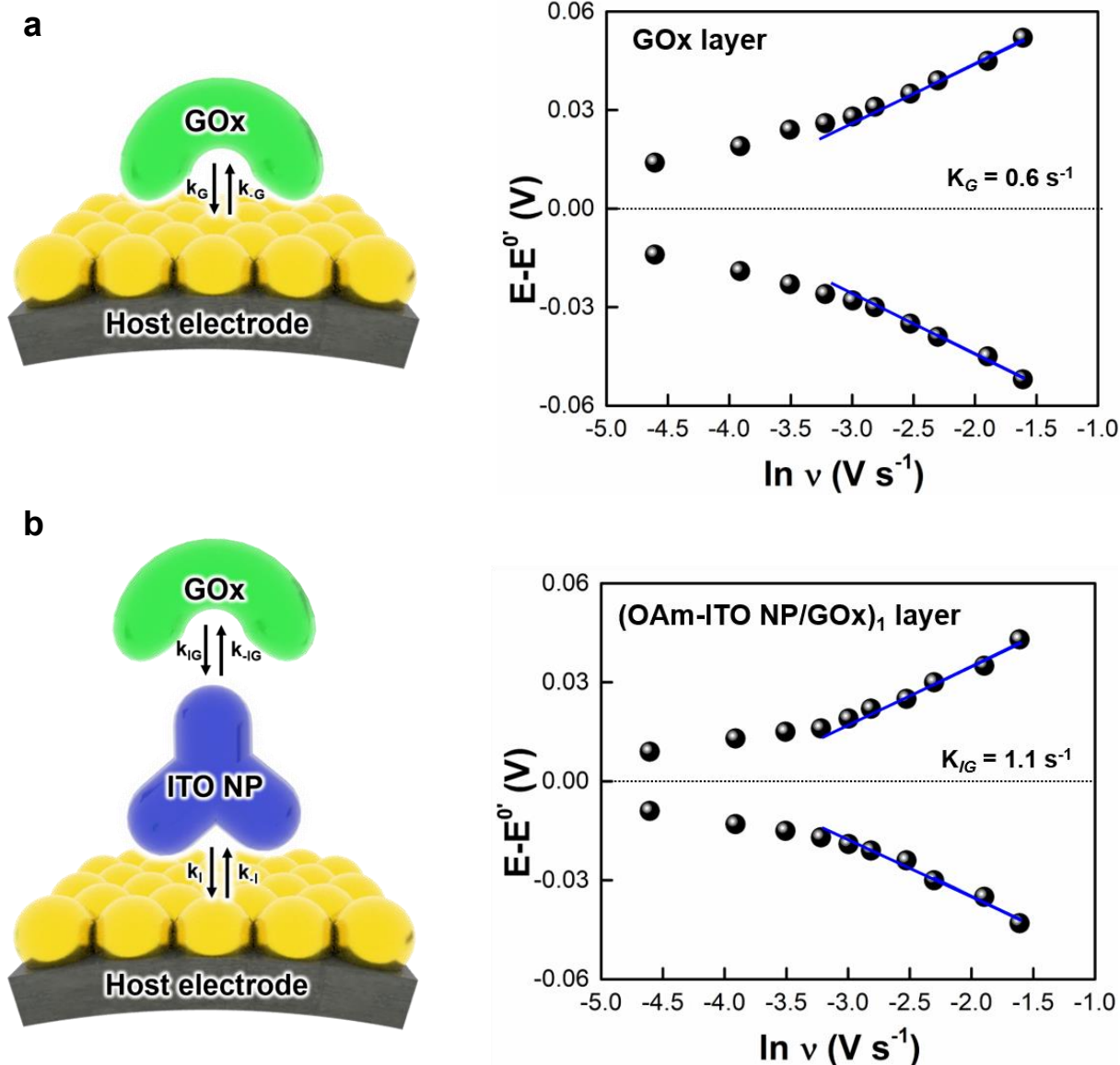


Figure S22. Change in the peak potential ($E-E^{0'}$) of a) GOx layer- and b) (OAm-ITO NP/GOx)₁ layer-coated host electrode (i.e., Au NP-coated Si wafer) as a function of $\ln \nu$. The GOx layer- and (OAm-ITO NP/GOx)₁ layer-coated host electrode exhibited a rate constant value of ~ 0.6 (K_G) and $\sim 1.1 \text{ s}^{-1}$ (K_{IG}), respectively. In case of (OAm-ITO NP/GOx)₁ layer, the two-step process is determined primarily by electron transfer between the GOx and the ITO NP (K_{IG}) as the rate-limiting step.

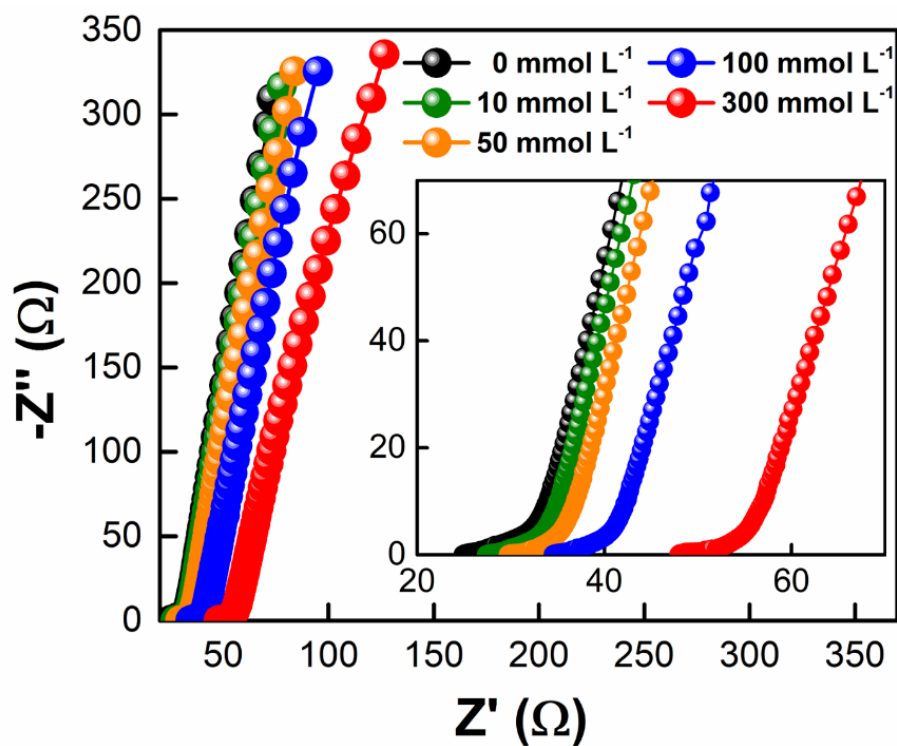


Figure S23. Nyquist plot of 5-anode as a function of glucose concentration in PBS with a pH of 7.4. The ESR values of the 5-anode for glucose concentration from from 0 to 300 mmol L^{-1} . The ESR values were increased from 25.8 Ω at 0 mmol L^{-1} , 30.1 Ω at 10 mmol L^{-1} , 30.6 Ω at 50 mmol L^{-1} , 35.3 Ω at 100 mmol L^{-1} , 47.1 Ω at 300 mmol L^{-1} glucose.

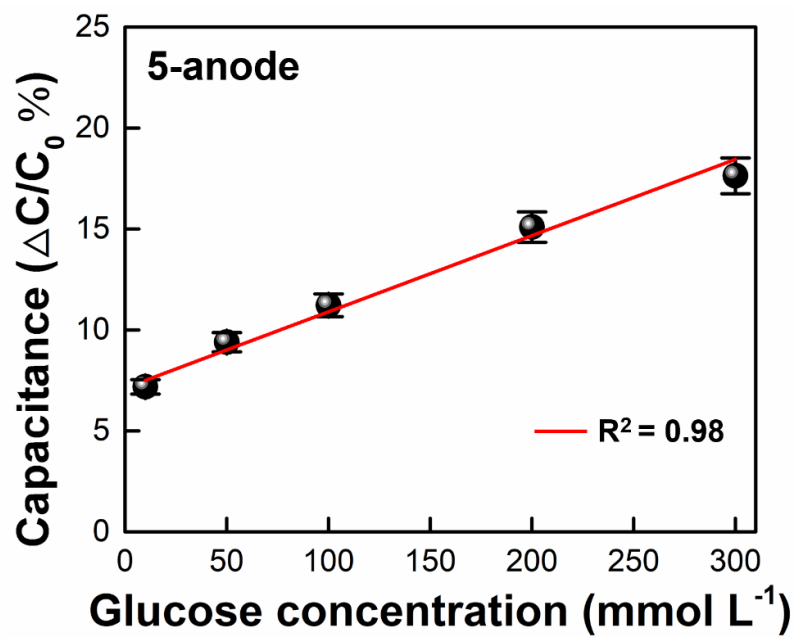


Figure S24. The calibration curve obtained by plotting relative change in interfacial capacitance as a function of glucose concentration.

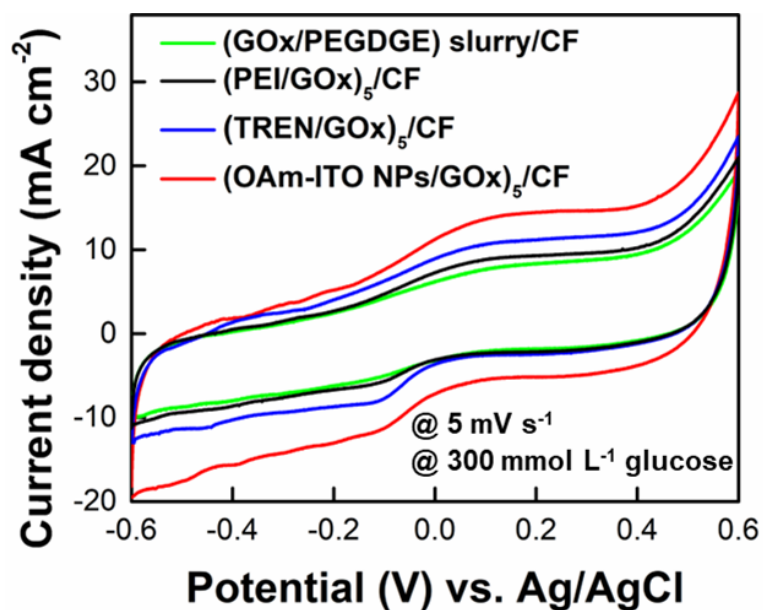


Figure S25. CV curves of GOx-based electrodes produced by crosslinking method ((GOx/PEGDGE) slurry/CF) and LbL assembly ((PEI/GOx)₅/CF, (TREN/GOx)₅/CF, and (OAm-ITO NPs/GOx)₅/CF). (GOx/PEGDGE) slurry/CF anode showed much lower anodic current densities than other LbL-assembled anodes due to the nonuniform coating.

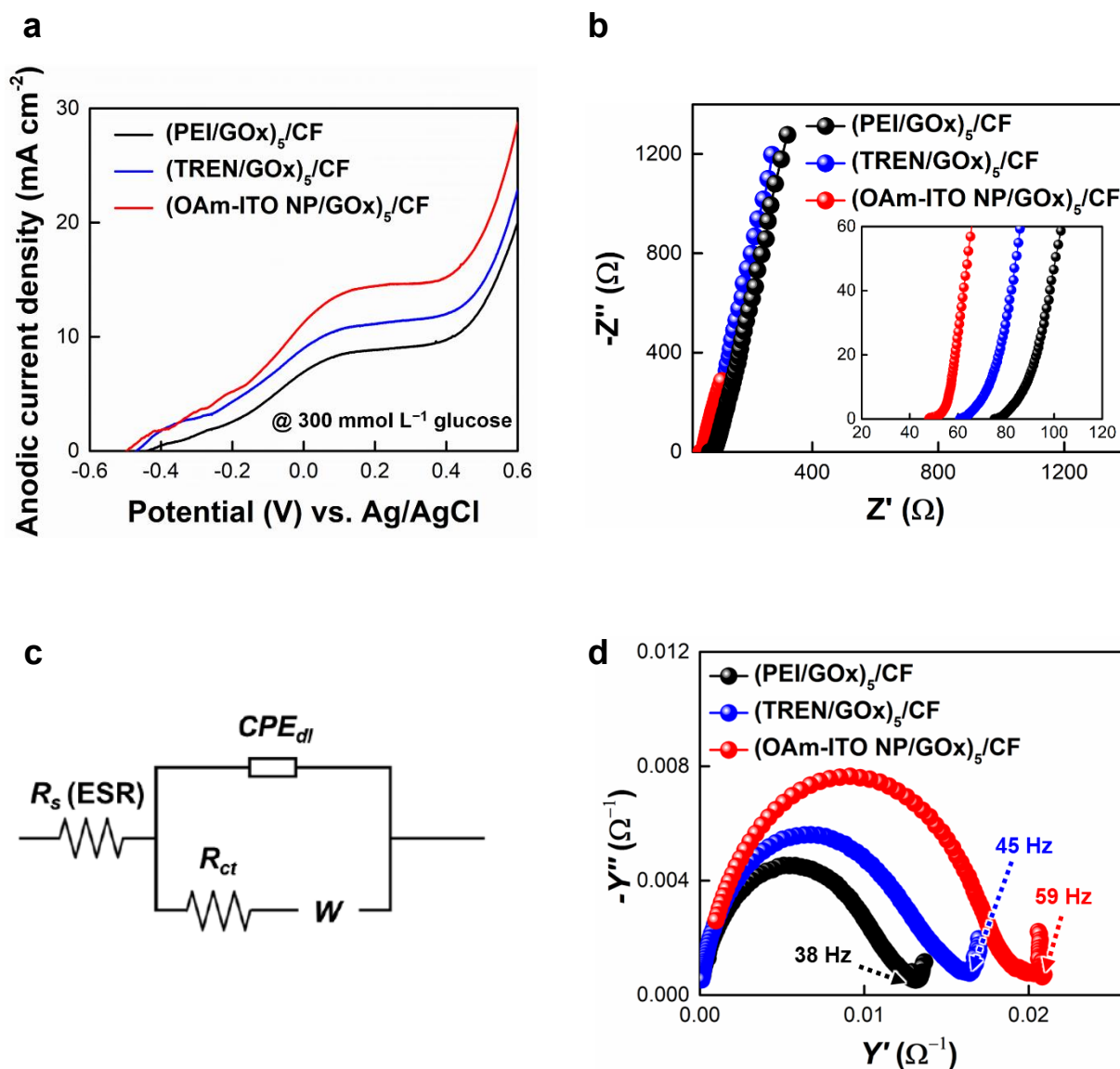


Figure S26. Electrochemical performances of multilayer thin films containing GOx and different linkers (OAm-ITO NPs, PEI, and TREN) on CF electrode. a) anodic current density curves of (OAm-ITO NP/GOx)₅/CF (i.e., 5-anode), (PEI/GOx)₅/CF, and (TREN/GOx)₅/CF. b) Nyquist curves. c) Representative equivalent circuit from the Nyquist plots in Figure S23b. d) Admittance plots that show the charge transfer rate related to the diffusion distance with knee frequency. The frequency values reflect the knee frequencies, which are defined as the crossover points from the charge transfer reaction to the diffusion-controlled region.

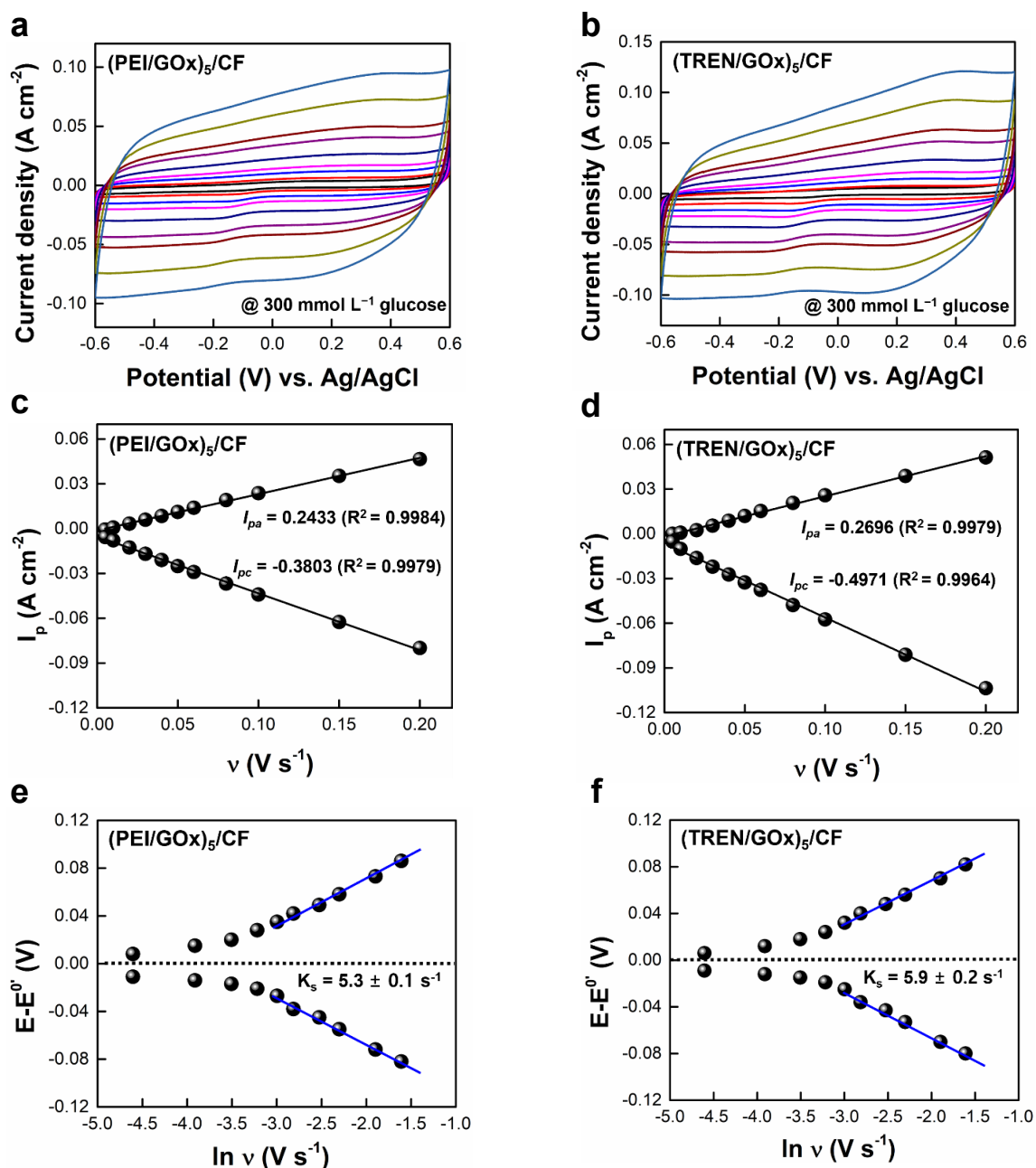


Figure S27. Electrochemical response of the of (PEI/GOx)₅/CF and (TREN/GOx)₅/CF. Cyclic voltammety curve of a) (PEI/GOx)₅/CF and b) (TREN/GOx)₅/CF in the 300 mmol L⁻¹ glucose in PBS at different scan rates 0.005, 0.01, 0.02, 0.03, 0.04, 0.05, 0.06, 0.08, 0.1, 0.15, 0.2 V s⁻¹, respectively. Change in the peak current of c) (PEI/GOx)₅/CF and d) (TREN/GOx)₅/CF with increasing the scan rate (ν) from 0.005 to 0.2 V s⁻¹. Change in the potential (E-E⁰) of e) (PEI/GOx)₅/CF and f) (TREN/GOx)₅/CF as a function of ln ν. The (PEI/GOx)₅/CF and (TREN/GOx)₅/CF exhibited a high K_s value of 5.3 ± 0.1 and 5.9 ± 0.2 s⁻¹.

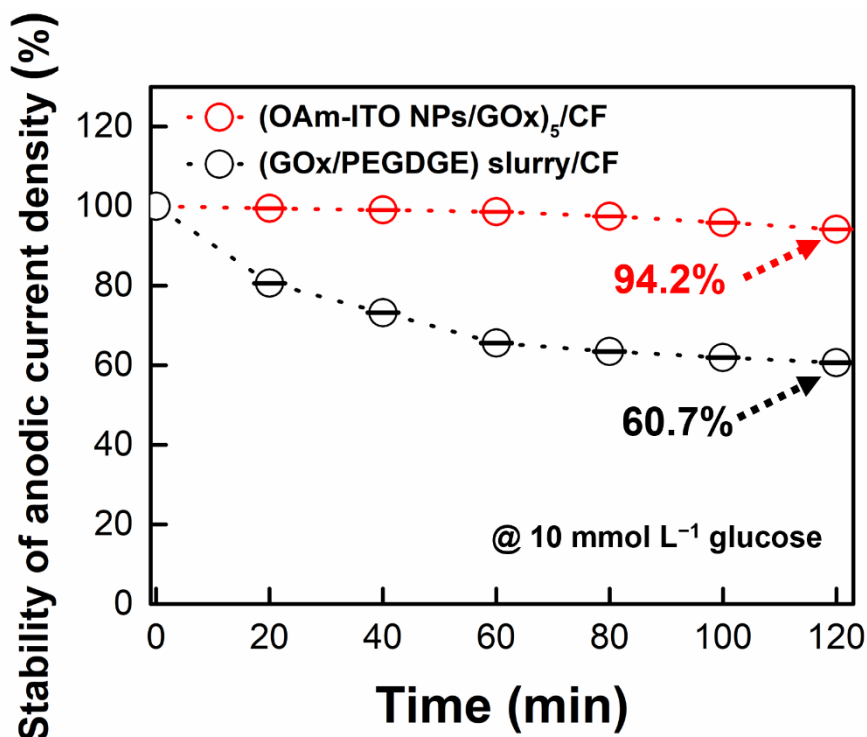



Figure S28. The retention of anodic current density (%) for (OAm-ITO NP/GOx)₅/CF anodes and conventional slurry-based (GOx-PEGDGE slurry/CF) anodes under continuous potential load of 0.6 V. (OAm-ITO NP/GOx)₅/CF maintained 94.2% of its initial current density after 2 hr, while (GOx/PEGDGE) slurry/CF only retained 60.7% of its initial current density due to adhesion failure in the PBS solution.

TEST REPORT

Table 1. Sample Information

No.	Sample Name	Koptri ID	Picture of the Sample
1	Conductive Fiber containing Indium tin oxide and glucose oxidase	Koptri-23-07-10705-2	

Note a) Sample morphology ; Solid : Powder (), Lump (O),
Liquid (pH) : Stock solution (), Solvent based solution (), Water based solution ()

Table 2. Test Result

Koptri ID	Test Item	Unit	Test Method	LOD	Test Result
Koptri-23-07-10705-2	Toluene	mg/kg	GC-FID	5	N.D.

Note)
a) mg/kg = ppm
b) Koptri-PB-VI20-SW0.1-EA-TH5
c) GC-FID ; Gas Chromatography – Flame Ionization Detection
d) LOD ; Limit of Detection
e) N.D. ; Not Detected

End of Test Report.

Figure S29. The amount of residual toluene within (OAm-ITO NP/GOx)₅/CF measured from GC-FID (Gas Chromatography – Flame Ionization Detection) at the Korea Polymer Testing & Research Institute (Koptri, Seoul, Korea). The residual toluene within (OAm-ITO NP/GOx)₅/CF anode prepared from our approach was not detected.

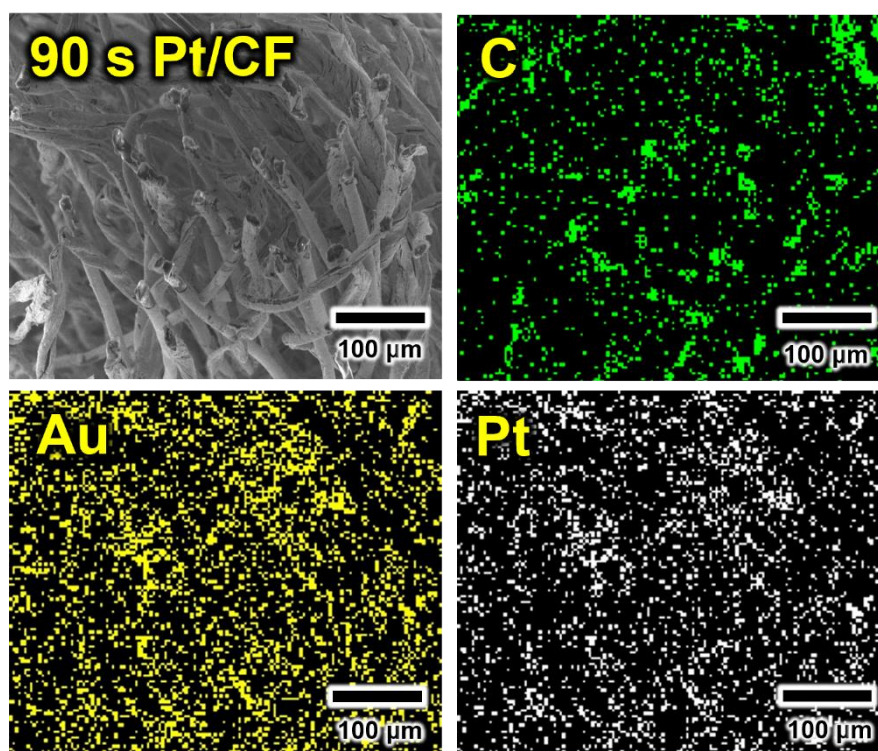


Figure S30. Surface morphology and elemental analysis of cathode. Cross-sectional FE-SEM and energy-dispersive X-ray spectroscopy (EDS) mapping images of Pt-sputtered CF.

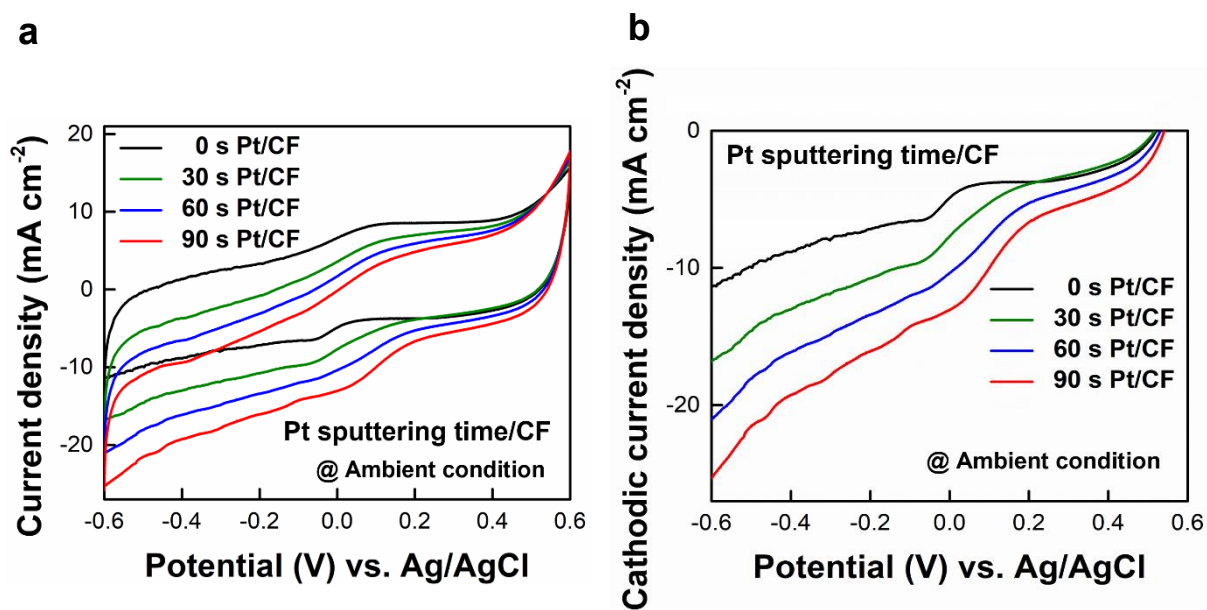


Figure S31. Electrochemical performance of Pt-sputtered cathode with increasing sputtering time from 0 to 90 s. The Pt-sputtered cathode was characterized by plotting a) CV curves and b) Cathodic current density curves as a function of Pt-sputtering time. All the electrochemical measurements were performed at a scan rate of 5 mV s⁻¹ in PBS under ambient condition.

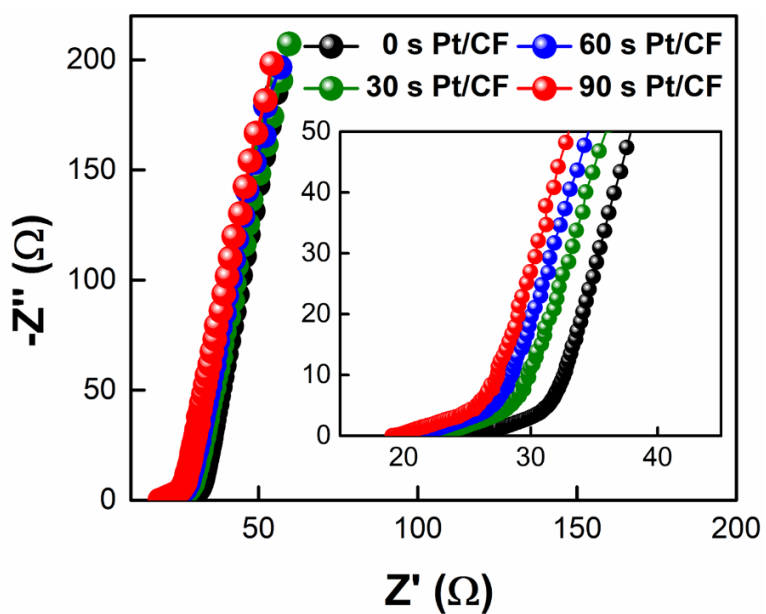


Figure S32. Nyquist plots of Pt-sputtered CF with increasing the sputtering time from 0 to 90 s. Inset: Nyquist plots magnified in the high-frequency range. In this case, the ESR value for time from 0 to 90 s were decreased from 25.8 to 19.8 Ω , respectively.

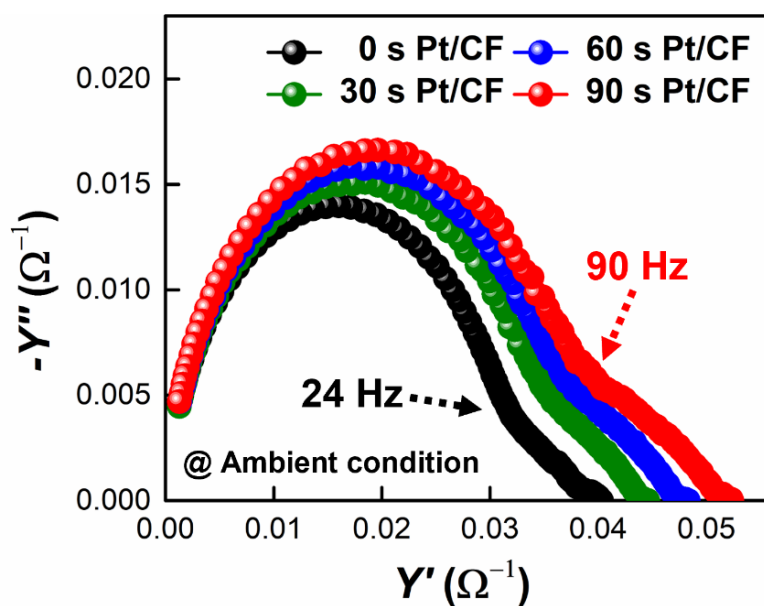


Figure S33. Admittance plots of Pt-sputtered CF with increasing the sputtering time from 0 to 90 s, with labeled frequency values indicating the knee frequency. Notably, the Pt/CF sample created via 90 seconds of sputtering exhibited a notably higher knee frequency (90 Hz) compared to those samples obtained via other sputtering time conditions (24 Hz for 0 s, 46 Hz for 30 s, 76 Hz for 60 s), which can be attributed to the improved charge transport kinetics.^[S11,S12]

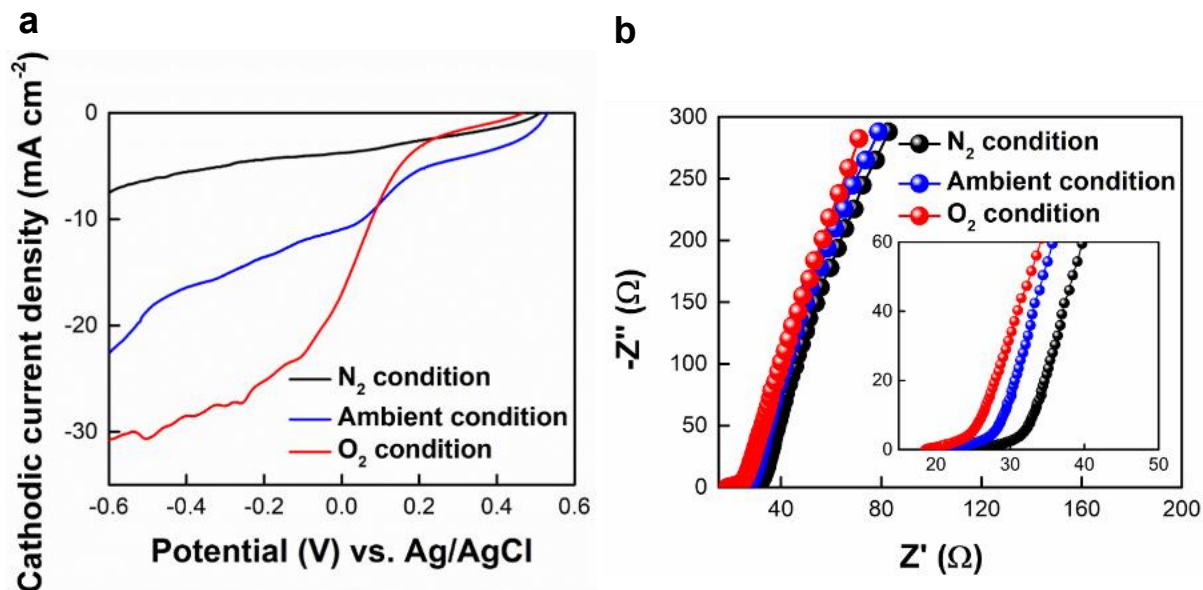


Figure S34. Electrochemical performance of 90 s Pt/CF under three different gas condition. a) Cathodic current density curves of Pt/CF under N₂-saturated, ambient conditions, O₂-saturated conditions. b) Nyquist plots of Pt/CF in the frequency range 0.2 Hz to 100 kHz were measured. Inset: Nyquist plots magnified in the high-frequency range. In this case, the ESR value were decreased from 26.7 to 19.4 Ω. All the electrochemical analysis were performed in PBS (pH 7.4) at 36.5 °C.

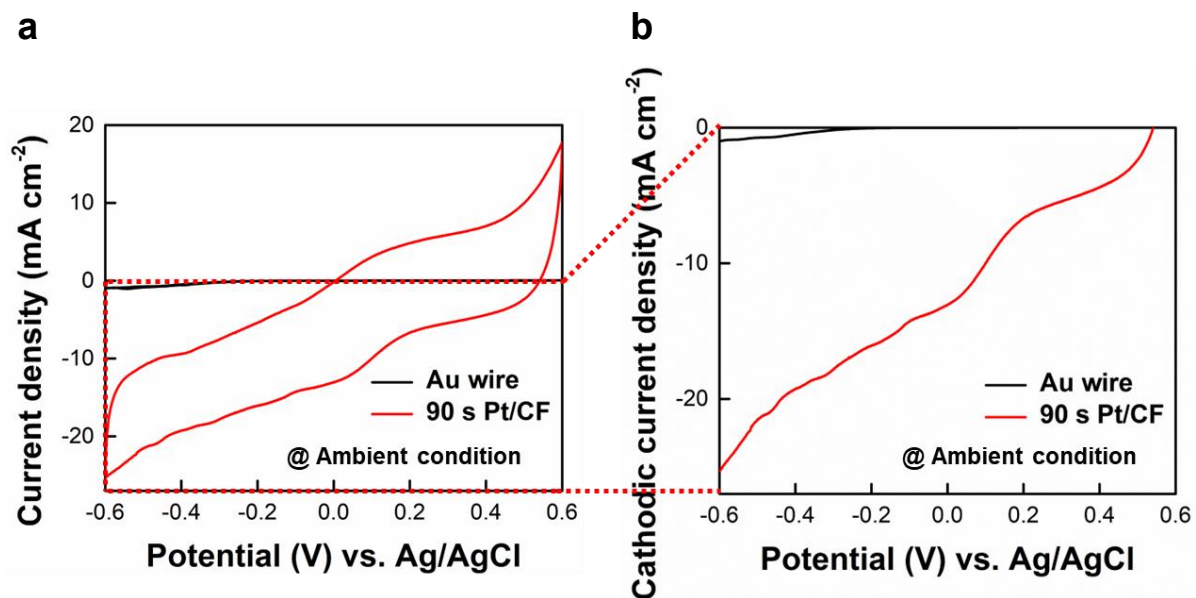


Figure S35. Electrochemical performance of nonporous bulk Au wire under ambient condition. a) CV curves and b) Cathodic current density curves of Au wire.

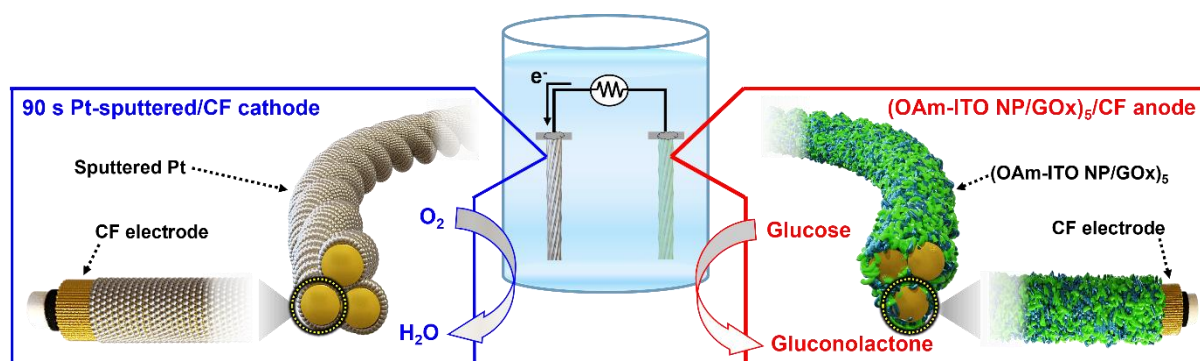


Figure S36. Schematic illustration of complete BFCs. (i.e., Anode: OAm-ITO NP/GOx)₅ multilayer-coated CF electrode, Cathode: 90 s Pt-sputtered CF).

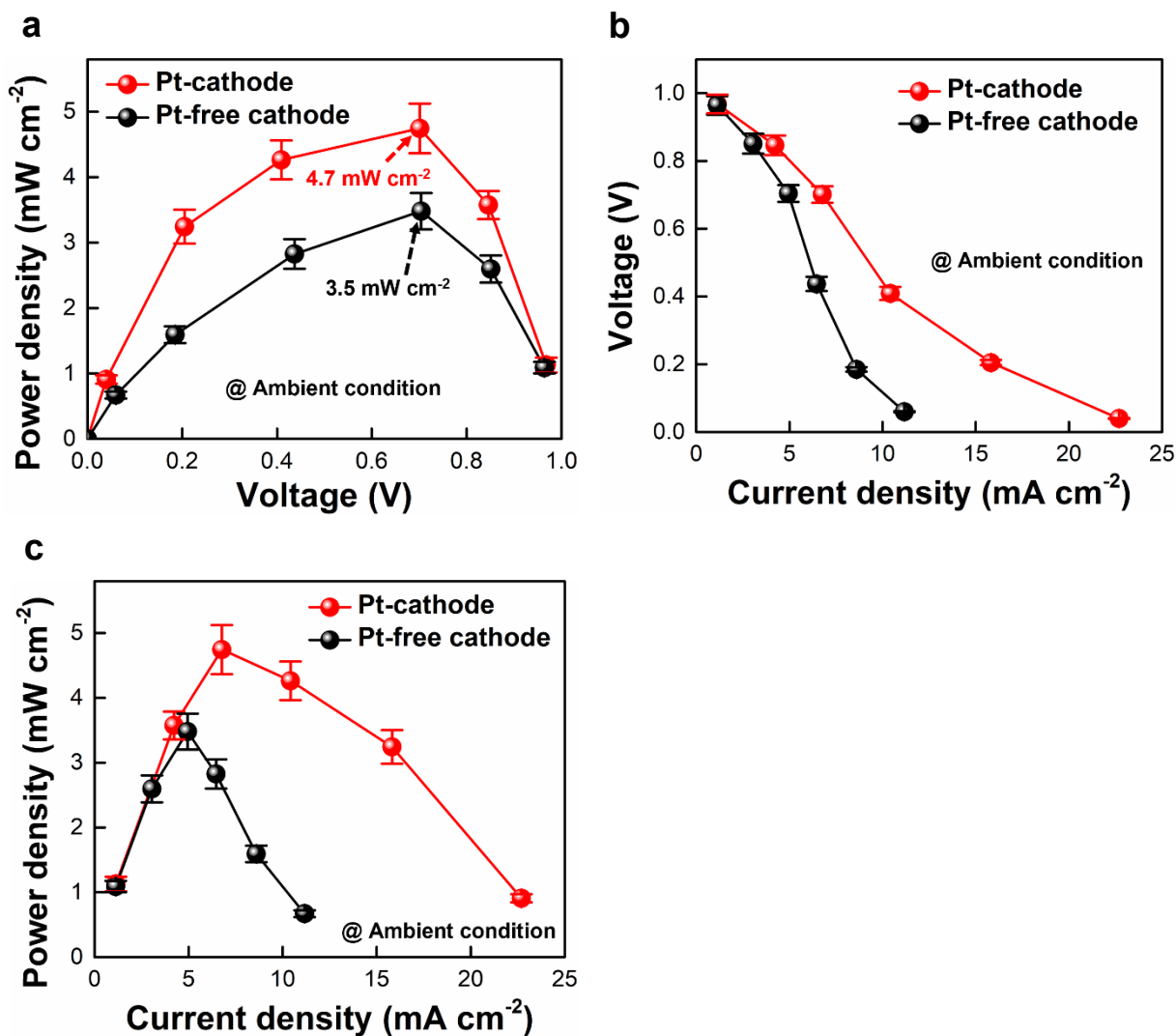


Figure S37. Effect of Pt-sputtered CF on power density. a) Power (P) – voltage (V), b) Voltage (V) – current (I), and c) Power (P) –current (I) profiles of the complete BFCs with two different types cathode (Pt-free and Pt-cathode). The BFCs operated in PBS solution under ambient condition at 36.5 °C.

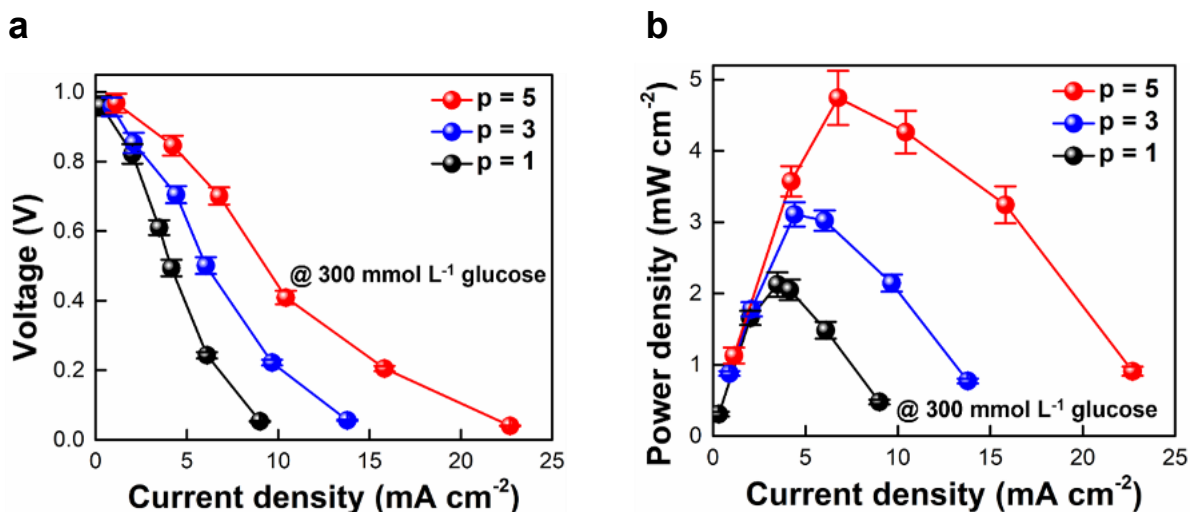


Figure S38. External load-based power output profiles of complete BFC in PBS solution containing 300 mmol L⁻¹ glucose. a) Voltage (V) – current (I) and b) Power (P) – current (I) profile profiles of the complete single BFCs. (i.e., Anode: p-anode, Cathode: 90 s Pt/CF). The power output was measured in PBS solution containing 300 mmol L⁻¹ glucose under ambient condition at 36.5 °C.

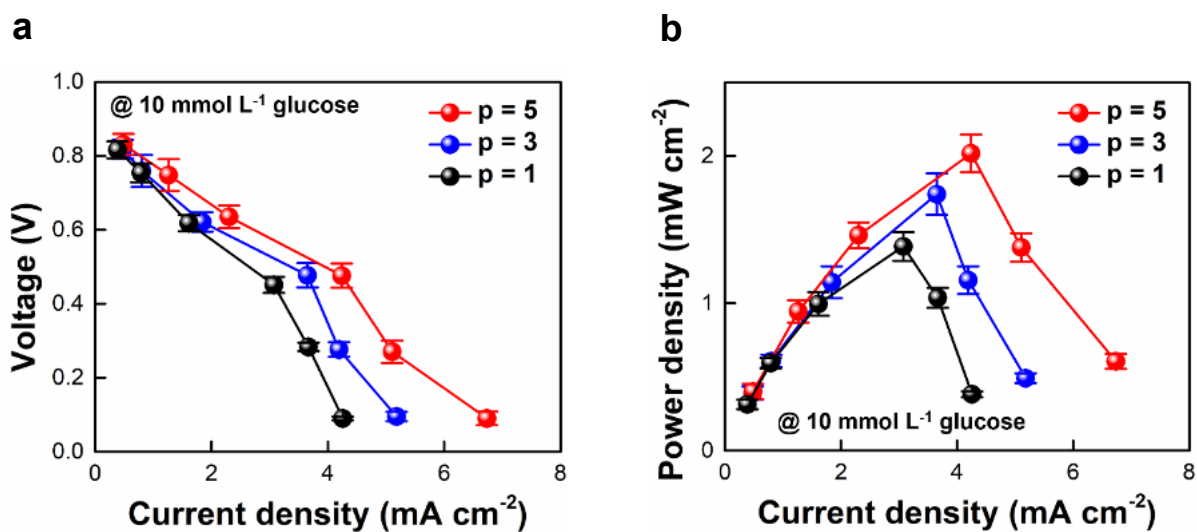


Figure S39. External load-based power output profiles of complete BFC in PBS solution containing 10 mmol L⁻¹ glucose. a) Voltage (V) – current (I) and b) Power (P) – current (I) profile profiles of the complete single BFCs. (i.e. Anode: p-anode, Cathode: 90 s Pt/CF). The power output was measured in PBS solution containing 10 mmol L⁻¹ glucose, under ambient condition at 36.5 °C.

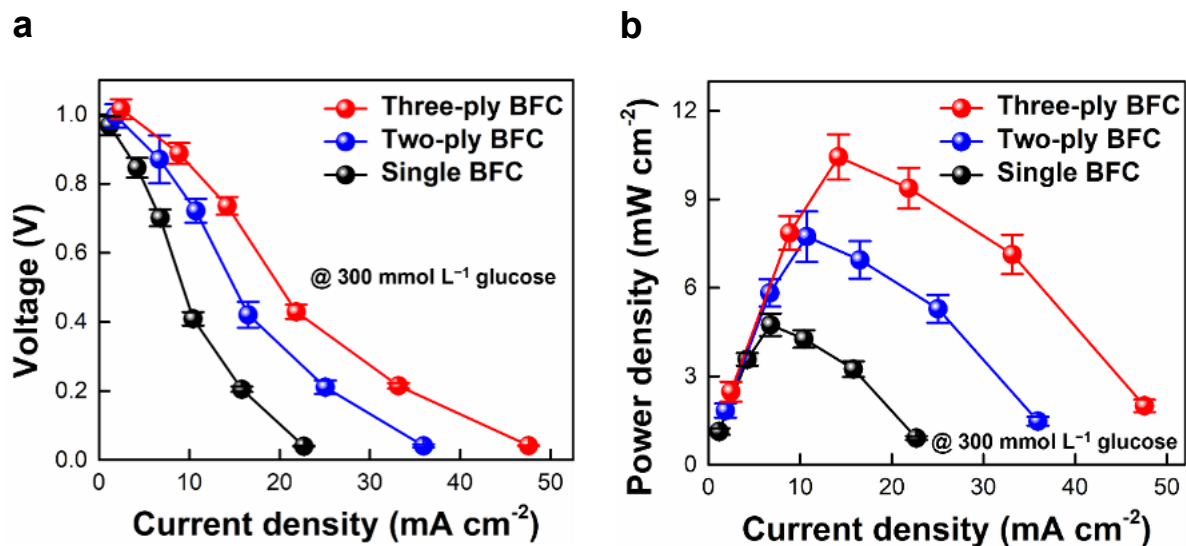


Figure S40. External load-based power output profiles of complete multi-ply BFCs. a) Voltage (V) – current (I) and b) Power (P) – current (I) profile profiles of the complete multiplied BFCs. (i.e., Anode: 5-anode, Cathode: 90 s Pt/CF). The power output was obtained in PBS solution containing 300 mmol L⁻¹ glucose under ambient condition at 36.5 °C.

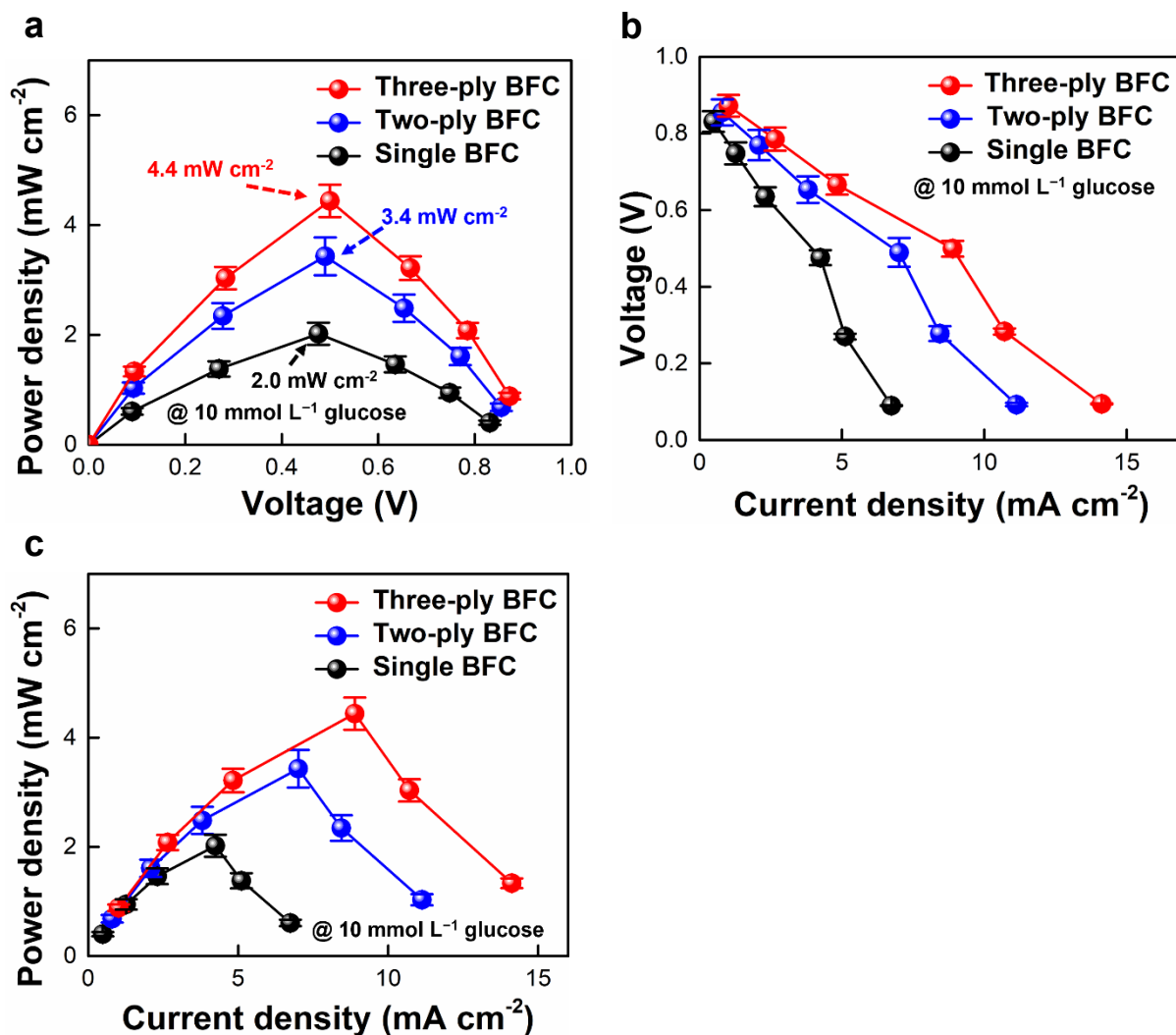


Figure S41. External load-based power output profiles of complete multi-ply BFCs. a) Power (P) – voltage (V), b) Voltage (V) – current (I) and c) Power (P) – current (I) profile profiles of the complete multi-plied BFCs. (i.e., Anode: 5-anode, Cathode: 90 s Pt/CF). The power output was obtained in PBS solution containing 10 mmol L⁻¹ glucose under ambient condition at 36.5 °C.

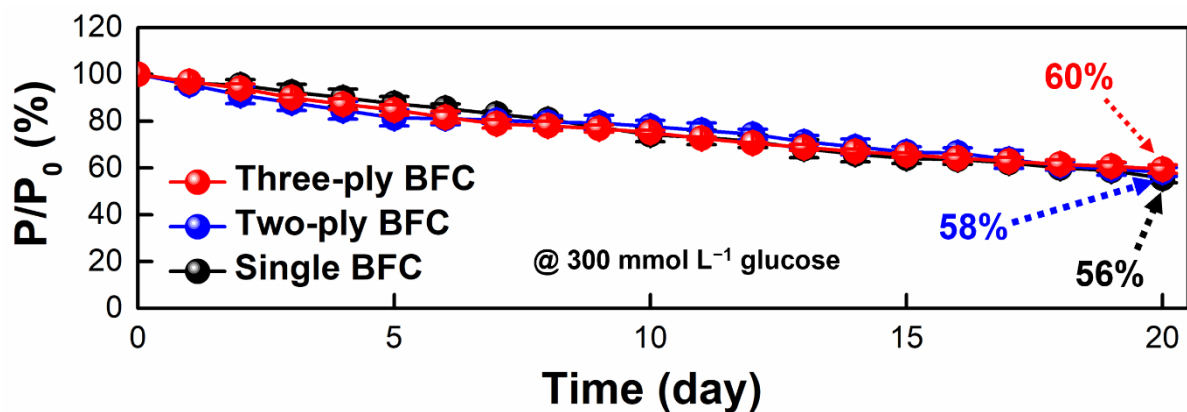


Figure S42. Relative power retention (P/P_0) of the complete multi-ply BFCs. The power output was obtained in PBS solution containing 300 mmol L⁻¹ glucose under ambient conditions at 36.5 °C. The power output was measured by controlling the cell potential through external variable resistors with values ranging from 1 k Ω to 10 G Ω .

Table S1. Power output performance of various fiber-type BFCs recently reported in the literature.

Host electrode	Maximum power density (mW cm ⁻²)	OCV (V)	Electron transfer	Stability	Ref.
CF	10.4 (three-ply) 4.7 (one-ply)	1.0	DET	49% (60 days) 45% (60 days)	Our work
GCE	1.1	0.5	DET	83% (14 days)	S13
CNTF	1.8	0.8	DET	84% (1 day)	S14
Carbon paper	0.3	0.6	MET	73% (30 days)	S15
Bucky paper	0.5	0.7	MET	–	S16
Carbon fiber	1.5	0.8	MET	–	S17
GCE	0.3	0.6	MET	–	S18
GCE	0.4	0.6	MET	56% (7 days)	S19
Carbon paper	2.6	0.8	DET	50% (7 days)	S20
Carbon fiber	0.3	0.6	MET	80% (12 h)	S21
CNT on rubber fiber	0.1	0.6	MET	52% (7 days)	S22
Screen-printed textile	0.1	0.7	MET	80% (6 h)	S23
Carbon fabric	1.0	0.7	DET	85% (1 day)	S24

Nickel foam	1.2	0.5	MET	90% (3 days)	S25
-------------	-----	-----	-----	--------------	-----

*GCE: Glassy carbon electrode

*CNTF: Carbon nanotube forest

References

- [S1] M. Brust, M. Walker, D. Bethell, D. J. Schiffrin, R. Whyman, *J. Chem. Soc. Chem. Commun.* **1994**, 801.
- [S2] H. Kanehara, H. Koike, T. Yoshinaga, T. Teranishi, *J. Am. Chem. Soc.* **2009**, *131*, 17736.
- [S3] I. Cho, Y. Song, S. Cheong, Y. Kim, J. Cho, *Small*, **2020**, *16*, 1906768.
- [S4] K. K. Kanazawa, J. G. Gordon, *Anal. Chem.* **1958**, *57*, 1770.
- [S5] M. Portaccio, B. Della Ventura, D. G. Mita, N. Manolova, O. Stoilova, I. Rashkov, M. Lepore, *J. Solgel Sci. Technol.* **2011**, *57*, 204.
- [S6] A. Barth, *Biochim. Biophys. Acta.* **2007**, *1767*, 1073.
- [S7] J. Bandekar, *Biochim. Biophys. Acta. Protein. Struct. Mol. Enzymol.* **1992**, *1120*, 123.
- [S8] S. Zhao, K. Zhang, Y. Bai, W. Yang, C. Sun, *Bioelectrochemistry* **2006**, *69*, 158.
- [S9] Y. Liu, J. Zhang, Y. Cheng, S. P. Jiang, *ACS omega* **2018**, *3*, 667.
- [S10] B. Dinesh, K. S. Shalini Devi, U. M. Krishnan, *ACS. Appl. Bio. Mater.* **2019**, *2*, 1740.
- [S11] R. M. Félix-Navarro, M. Beltrán-Gastélum, E. A. Reynoso-Soto, F. Paraguay-Delgado, G. Alonso-Nuñez, J. R. Flores-Hernández, *Renew. Energy.* **2016**, *87*, 31.
- [S12] S. B. Yoon, J. P. Jegal, K. C. Roh, K. B. Kim, *J. Electrochem. Soc.* **2014**, *161*, H207.
- [S13] Z. Kang, K. Jiao, J. Cheng, R. Peng, S. Jiao, Z. Hu, *Biosens. Bioelectron.* **2018**, *101*, 60.
- [S14] T. Miyake, S. Yoshino, T. Yamada, K. Hata, M. Nishizawa, *J. Am. Chem. Soc.* **2011**, *133*, 5129.

- [S15] P. Gai, R. Song, C. Zhu, Y. Ji, Y. Chen, J. -R. Zhang, J. -J. Zhu, *Chem. Commun.* **2015**, 51, 14735.
- [S16] X. Chen, L. Yin, J. Lv, A. J. Gross, M. Le, N. G. Gutierrez, Y. Li, I. Jeerapan, F. Giround, A. Berezovska, R. K. O'Reilly, S. Xu, S. Cosnier, J. Wang, *Adv. Func. Mater.* **2019**, 29, 1905785.
- [S17] H. Sakai, T. Nakagawa, Y. Tokita, T. Hatazawa, T., Ikeda, S. Tsujimura K. Kano, *Energy Environ. Sci.* **2009**, 2, 133.
- [S18] Y. Yu, M. Xu, L. Bai, L. Han, S. Dong, *Biosens. Bioelectron.* **2016**, 75, 23.
- [S19] Z. Zhong, L. Qian, Y. Tan, G. Wang, L. Yang, C. Hou, A. Liu, *J. Electroanal. Chem.* **2018**, 823, 723.
- [S20] K. So, S. Kawai, Y. Hamano, Y. Kitazumi, O. Shirai, M. Hibi, J. Ogawa, K. Kano, *Phys. Chem. Chem. Phys.* **2014**, 16, 4823.
- [S21] S. Yin, X. Liu, K. Kaji, Y. Nishina, T. Miyake, *Biosens. Bioelectron.* **2021**, 179, 113107.
- [S22] H. J. Sim, D. Y. Lee, H., Kim, Y. -B. Choi, H. -H. Kim, R. H. Baughman, S. J. Kim, *Nano Lett.* **2018**, 18, 5272.
- [S23] W. Jia, X. Wang, S. Imani, A. J. Bandodkar, J. Ramírez, P. P. Mercier, J. Wang, *J. Mater. Chem. A* **2014**, 2, 18184.
- [S24] T. Miyake, K. Haneda, S. Yoshino, M. Nishizawa, *Biosens. Bioelectron.* **2013**, 40, 45.
- [S25] M. Sakthivel, S. Ramaraj, S.-M. Chen, T.-W. Chen, K. -C. Ho, *ACS Appl. Mater. Interfaces*, **2019**, 11, 18483.